Observations of Stress-Strain in Drifting Sea Ice at Floe Scale

Julie Parno[1], Chris Polashenski[1,3], Matthew Parno[3], Tricia Nelsen[1], Andrew Mahoney[2], Arnold Song[3]

[1]Cold Regions Research and Engineering Laboratory, U.S. Army Corps of Engineers, Hanover, NH

[2]University of Alaska Fairbanks, Fairbanks, AK

[3]Dartmouth College, Hanover, NH

Corresponding author: Julie Parno (Julie.T.Parno@usace.army.mil)

Key Points:

- Stress-strain measurements at the scale of a sea ice floe are presented for the first time, capturing the formation of a lead
- Fractures are observed hours before lead opening and may be pre-indicated by high-strain regions, providing avenues to fracture forecasting
- Failures are consistent with compressive shear faulting and tensile crack elongation, but occur well below expected failure stress criteria

Abstract

The mechanical deformation of sea ice has substantial influence over large-scale (e.g., >10 km) ice properties, such as the ice thickness distribution, as well as small-scale (e.g., <50 m) features, including leads and ridges. The conditions leading to sea ice fracture are frequently studied in the context of a uniform ice sheet. Natural sea ice, however, is highly heterogeneous and riddled with flaws. Failure occurs primarily as brittle fracture localized in space and time where stresses, and strain rates, locally exceed failure criteria. Here we seek to better understand the mechanical deformation and fracture of sea ice under such typical field conditions. In particular, we aim to characterize how forces propagate across an approximately 1 km^2 heterogeneous domain by observing the stress-strain field in an ice floe at resolutions required to capture pre-fracture elastic strains. The combination of instruments deployed allow a detailed view of the formation, propagation, parting, and subsequent shearing of a fracture in natural sea ice, providing field evidence of modes of failure in compressive shear. The relatively low change in stress observed within meters of the fracture location highlights the need for further research into disparities in sea ice strength measurements at laboratory and field scales. The ability of this system to capture strain concentration zones and to detect initial fracture hours prior to lead formation indicates the potential for predicting areas at high risk for fracture in an on-ice operational setting.

Plain Language Summary

A key attribute of the polar sea ice pack is that it moves and fractures. The details of how sea ice fractures are still poorly understood, limiting our ability to predict ice motion and the safety of ice. We hypothesized that fractures occur due to local stress concentration and that the locations where this happens are controlled by the shape, thickness variability, and orientation of ice floes interacting. To look closer at how fractures form, we deployed a system of instruments that measure the stress and strain of the ice over an approximately 1 km^2 area. With this system, we captured the moment when a fracture formed and spread through the ice, allowing us to view how and why it fractured in detail. We found that the ice fractured under less stress than would be expected from laboratory experiments, a topic that requires additional research. We also observed some indications of the fracture prior to lead formation, offering hope that the system deployed can help predict future fracture locations. Finally, we observed that the character of the ice failure was consistent with prior studies conducted at laboratory scale, providing support for the present understanding of the modes of fracture.

1 Introduction

Sea ice extends over 14 million square kilometers of the Arctic Ocean in winter, governing ocean-atmosphere heat exchange, impacting human navigation, and providing essential services in an ice-adapted ecosystem (Inoue, 2020; Kurtz et al., 2011; Stroeve & Notz, 2018). The sea ice is highly dynamic, drifting and deforming under the influence of winds and ocean current forces. Such mechanical deformation exerts substantial control over the large-scale ice thickness distribution, the rates of ice drift, the size of ice floes, and the extent of winter open water (B. J. Lewis & Hutchings, 2019; Thorndike et al., 1975). For those operating in the Arctic pack ice, lead formation (divergence) and ridge building (convergence) can ease or restrict navigation and pose a risk to structures over very short timescales. It is therefore desirable to improve our ability to understand, model, and predict the deformation and drift of sea ice. One critical step in achieving this capacity is to better understand how stress is transmitted through the ice pack and under what criteria ice fractures occur.

Ice mechanics are well studied at laboratory scale, <O(1 m), through highly controlled experimentation (Schulson & Duval, 2009), and ice deformation has been extensively observed over large scales >O(10 km) by means of buoy arrays and satellite remote sensing (Weiss, 2013). Comparatively little is known about deformation on intermediate scales (e.g., 1 m - 10 km). The authors here are not aware of any stress-strain observations of temporal and spatial fidelity necessary to observe rheology leading up to fracture at a floe scale O(1 km). Some key differences are expected between ice behavior at floe scale and in laboratory settings, most particularly that the natural ice is highly likely to have substantial heterogeneity in strength, thickness, and stress state at the floe scale, but also that flexural modes of failure become increasingly feasible as the aspect ratio of the ice increases. In a natural ice field, it is expected that individual fracture events are controlled by the interaction of spatial and temporal variability in ice strength with internal ice stress state, both of which likely vary more greatly than would be expected within most laboratory-scale samples (Weiss et al., 2007).

Prior observations of ice deformation outside of a laboratory setting have primarily been acquired through satellite remote sensing, GPS buoy arrays, and ground-based marine radars. Remote sensing data of varying modes and resolutions allow analysis of the strain field over large areas; ranging from about 10 x 10 km to the entire Arctic basin (Marsan et al., 2004), albeit with significant limitations on temporal resolution. A particularly well-developed body of work has used the RADARSAT Geophysical Processor System (RGPS) dataset, which uses synthetic aperture radar (SAR) imagery from the Canadian RADARSAT satellite and feature-tracking techniques to determine ice motion over time (Bouchat & Tremblay, 2017; Kwok et al., 2008; Lindsay et al., 2003; Marsan et al., 2004; Spreen et al., 2017; Xie et al., 2017). Interferometric SAR (InSAR) techniques have been used to observe cm-scale deformation of sea ice and associated fractures (Dammann et al., 2018; Li et al., 1996). However, such work has been largely limited to studies of landfast ice since orbital repeat intervals are typically on the order of several days and the typical drift rate of moving pack ice leads to coherence loss in a matter of minutes. Mahoney et al. (2016) demonstrated the use of TanDEM-X InSAR with a 10-second repeat interval to observe vertical motion and horizontal deformation in drifting sea ice, but such data were available only for a short period during the TanDEM-X mission. Buoy arrays also provide an opportunity to determine strain rates at higher temporal resolution, but GPS position quality limits the accuracy of these arrays at scales below O(10km^2) (Hutchings et al., 2010;

Hutchings & Hibler, 2008; Itkin et al., 2017; Rampal et al., 2008). More recently, ship and ground-based radar systems have successfully resolved deformation measurements at high temporal frequency with meter scale resolutions (Jones et al., 2016; Lund et al., 2018; Oikkonen et al., 2016). With the exception of interferometry-based approaches, all of these techniques are limited in their ability to resolve strains at the scale of individual fractures. Moreover, although there has been recent progress in the application of terrestrial radar interferometry on drifting sea ice (Dammann et al., 2021), none of these techniques is able to show elastic, plastic, or creep deformation within monolithic ice floes prior to fracture, which would provide information analogous to laboratory scale ice block failure testing.

Observing the sea ice internal stress state in a natural setting is difficult. Observations are limited to point measurements using embedded strain gages (Coon et al., 1993; Cox & Johnson, 1983; Hata & Tremblay, 2015; Johnson, 1985; Richter-Menge et al., 2002; Richter-Menge & Elder, 1998; Templeton, 1980; Tucker & Perovich, 1992). Richter-Menge and Elder (1998) monitored ice stresses at the edge and center of a multiyear ice floe in the Beaufort Sea, Alaska and found significant temporal and spatial variability in stresses, especially compressive stress, within a single floe. Lewis and Richter-Menge (1998) compared motion-induced stresses from stress gage data collected in the Beaufort Sea to residual stresses calculated from a force balance approach and found discrepancies between modeled and point observations of stresses, indicating that the residual stresses were not locally generated. These studies together suggest that the propagation of far-field stress through a natural ice cover is heterogeneous and stress concentration by floe contact geometries and strength heterogeneities likely govern ice failure. Very few studies to date have obtained contemporaneous ice stress and strain measurements and none at the resolution needed to observe crack formation and local propagation.

Just as buoy and remote sensing observations measure large-scale deformation occurring across an aggregation of failure sites, the majority of sea ice deformation models represent the ice as a continuum and capture aggregate large-scale dynamics with constitutive relationships like the viscous-plastic rheology (Hibler, 1979). These models, while computationally efficient, treat brittle failure and relative ice motion as aggregate processes, and do not explicitly capture fine-scale variability in the stress state or the numerous discrete fracture events that comprise real-world deformation (Rampal et al., 2008; Weiss et al., 2007). These approximations limit the utility of many continuum models to scales where many individual fractures can be treated as a statistical process. Elasto-brittle rheologies provide more realistic failure criteria, but still do not capture individual small-scale fracture events (Dansereau et al., 2016). As small-scale discrete element methods emerge and become feasible in sea ice modeling, more observations of individual failure criteria and floe-floe interactions are needed for model validation and calibration (Damsgaard et al., 2018; Herman, 2016; Hopkins, 2004; Wilchinsky et al., 2011).

In this study, we aim to take a first step toward these types of observations, testing a unique combination of instruments to capture sea ice strain and stress in an approximately 1 km^2 area on the sea ice in the Beaufort Sea north of Prudhoe Bay, Alaska. The relatively fine scale of the dataset allows us to examine the ice dynamics in detail during failure events. Contemporaneous strain and stress measurements have not previously been performed at this scale and their relationship provides further insight into sea ice constitutive behavior.

2 Data and Methods

Observations were collected on drifting sea ice in the Beaufort Sea approximately 230 km north of Prudhoe Bay, Alaska from 08 to 21 March 2018 as part of the U.S. Navy Ice Camp Skate. The camp was established at approximately 72°N 142°W on a multiyear ice (MYI) floe directly adjacent to level first year ice (FYI), upon which the camp runway was constructed. The instrumentation array was designed to monitor ice stress and strain at the scale of an ice floe, O(1 km^2). At the beginning of the campaign, the entire study domain was behaving as a contiguous, monolithic floe, and no recently active flaws were noted. During the study period, the ice came under stresses that resulted in failure. A crack formed, opened, closed, sheared, and further deformed within the study domain, providing a test case for examining stress-strain state in the ice prior to, during, and after failure.

Floe-scale strain was measured using a Leica TM50 high precision robotic total station positioned on a large multiyear pressure ridge, measuring movements of an array of 23 prismatic retro-reflectors, each mounted on a steel post rigidly embedded in the ice (Figure 1). The 23 posts were installed at ranges from 47 m to 891 m from the base station, and spaced through 360 degrees of azimuth. Measurements of the relative position of each reflector were made every 1 to 2 minutes, depending on the length of time required for the instrument to complete a cycle locating each reflector. Laser ranging data is corrected for atmospheric effects on pulse time-of-flight according to Leica's instructions. Laser pointing data is corrected for angular encoder drift by using the average movement of a group of 'master' points on the heavy MYI, which are expected to have minimal angular motion. The results, therefore constitute motion relative to the position of the scanner, as oriented relative to the master points. The stated strain accuracy of the system is approximately 1.6 $x10^{-6}$ (0.6mm +1mm/km absolute range displacement, 1.4 x 10^{-4} degree absolute angular displacement). Field performance is likely lower due to complex lower atmosphere conditions at the site, such as inversions, but still appears to be considerably better than 10^{-5}, based on consistent repeated observations of points over times with minimal observed stress. At this level, the resolution of the technique allows for the detection of elastic strains that would be expected from stresses of O(10 kPa) or smaller, based on the ice having a Young's modulus of O(10 GPa).

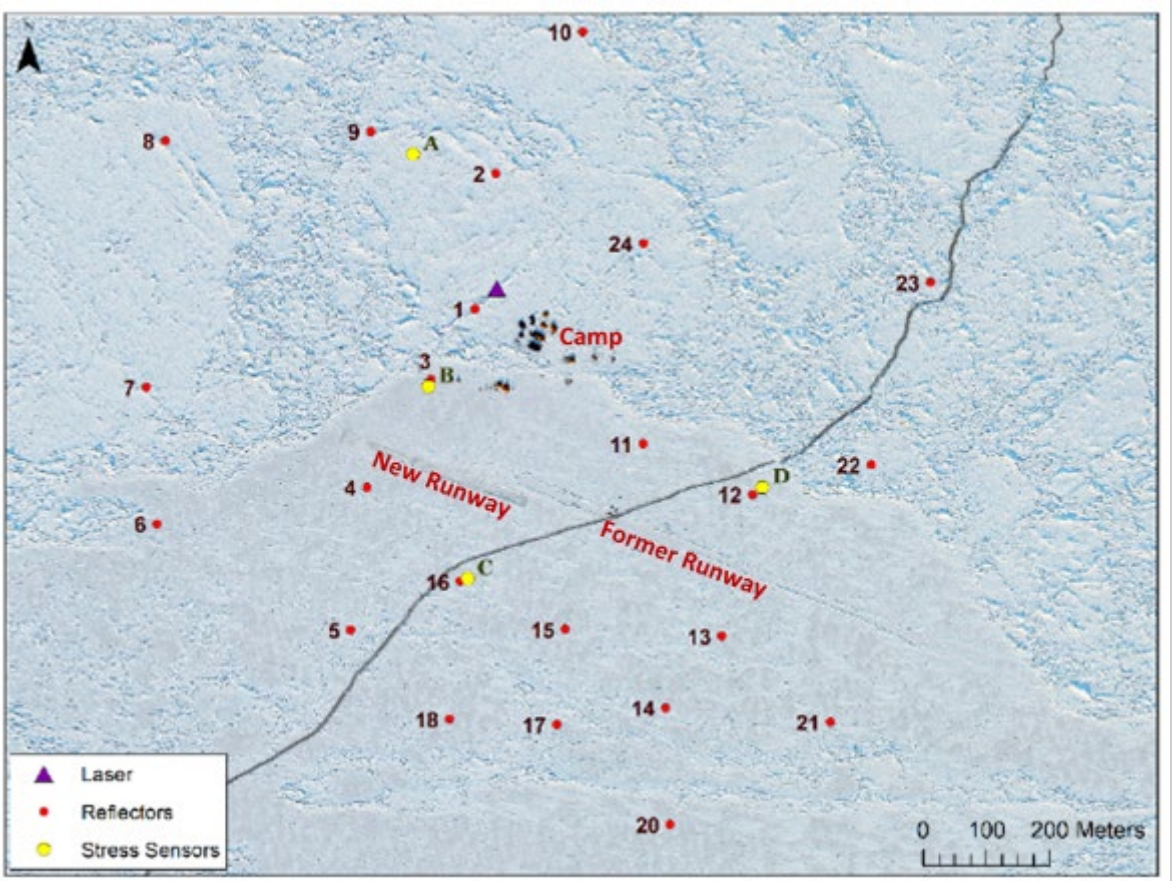

Figure 1. Overview of the study site at Ice Camp Skate, 13 March 2018, after a fracture occurred through the site. The robotic total station (purple triangle) is just northwest of camp and situated among an array of reflectors (red circles). The stress sensor locations (yellow circles) are noted. Imagery © 2018, DigitalGlobe, Inc., NextView License.

Additionally, four vibrating wire stress gages were deployed to collect point observations of internal ice stress (Cox & Johnson, 1983), with their rosettes positioned at 25 cm below the ice surface (Table 1). The sensors measure the resonant frequency of a rosette of wires stretched across a hollow steel cylinder embedded in the ice to measure changes in the cylinder diameter, caused by stress on the cylinder. Stress is estimated using a series of calculations that account for the inclusion factor in the ice, which are fully described in Cox and Johnson (1983). Each sensor is equipped with a thermistor to provide the ice temperature at the point of the stress sensor and correct for thermal expansion impacts on the wire resonant frequency. Snow-ice interface temperature was also observed prior to gage installation using an Omega THX-400 handheld temperature probe. Stress is provided as primary and secondary principal stresses, along with the angle of primary principal stress relative to the installation orientation. Challenges with this sensor type give us relatively low confidence in the absolute magnitude of stresses observed – for example because expansion during freeze-in can create pressures in the immediate area surrounding the sensor, or because the extremely rigid sensor (poorly matching the modulus of the surrounding ice) can load the surrounding ice and encourage creep relaxation over time. These challenges of measuring stress in ice over long periods are reviewed in Cox and Johnson (1980), who estimate long-term errors on the order of 20%. The sensors, are, however, quite

responsive and therefore capable of observing short-term relative changes in stress, and this will be our primary use of the data. In this study, we use the convention that compressive stresses are positive. We note that, since the absolute magnitude of stress state is impacted by local freeze-in stresses, the zero-stress reference is, to a degree, ambiguous. Increasingly positive stress values are therefore possibly either more compressive, or less tensile stresses.

Table 1. Ice properties at the location of each stress sensor, collected during recovery of sensors on 21 March 2018.

Stress Sensor	Ice Type	Ice Thickness (cm)	Ice Temperature at Snow-Ice Interface (°C)
A	Multiyear	354	-17.6
B	First Year	101	-13.0
C	First Year	100	-12.8
D	First Year	98	-13.3

Two GNSS logging stations were installed on the drifting ice to enable correction of all georeferenced data to a common ice-fixed coordinate system across all observations. For visualization purposes, this reference frame was fixed to the collection time of a WorldView-3 satellite image from 21 March 2018. These drifting coordinates were used to support observations characterizing the ice geometry within the boundaries of the reflector array. Snow depth and ice thickness were recorded along several transects, covering the majority of the straight-line routes between reflectors, and containing a representative sample of both MYI and FYI. The snow depth data were collected opportunistically at irregular intervals, the majority being 1-5 m apart, along the transect at approximately 5 cm accuracy with a Magnaprobe (Sturm & Holmgren, 2017). The ice thickness data were recorded every 5 seconds while walking the transects to approximately 0.1 m accuracy using a Geonics EM31 ground conductivity meter (Echert et al., 1992; Kovacs & Morey, 1991). The regional ice dynamics outside of the reflector array were tracked using repeat satellite imagery, both optical (WorldView -2 and -3) and SAR (from TerraSAR-X and CosmoSkyMed).

To help assess when the ice started to fracture, a quasi-static linear elastic finite element model of the ice was constructed and used within a Bayesian model calibration framework. This allows us to test whether the observed displacements are well represented by elastic ice deformation alone, or if it is likely that fracture has occurred. Spatially variable displacement boundary conditions were calibrated so that predicted displacements match displacements observed at the laser reflectors. Taking a Bayesian approach also enabled the uncertainty in the laser measurements to be accounted for. Quantitative Posterior predictive tests (Bayesian p-values) were used to assess whether the linear elastic model was a good approximation of the observed ice deformation during different time periods, thus providing quantitative support for our hypothesized ice fracture timeline. Details of the finite element model and Bayesian analysis can be found in the appendix.

3 Results

3.1 Description of Site and Failure Events

The sea ice in the area around Ice Camp Skate was composed of both FYI and MYI. The MYI was primarily found within discrete floes, which were actually conglomerates of deformed MYI with highly deformed first year inclusions (bright areas in the SAR image shown in Figure 2). A band of such floes running E-W, approximately 100 km wide from N-S, was circulating in the Beaufort Gyre approximately 200-300 km north of the Alaska Coast at the time of the camp. Within the band, the isolated multiyear conglomerate floes were surrounded by a matrix of predominantly FYI. Outside the band, ice in the southern Beaufort was almost exclusively FYI at the time. An overview Sentinel-1 image is shown in Figure 2, along with an inset of the approximately 50 x 50 km^2 area around the camp.

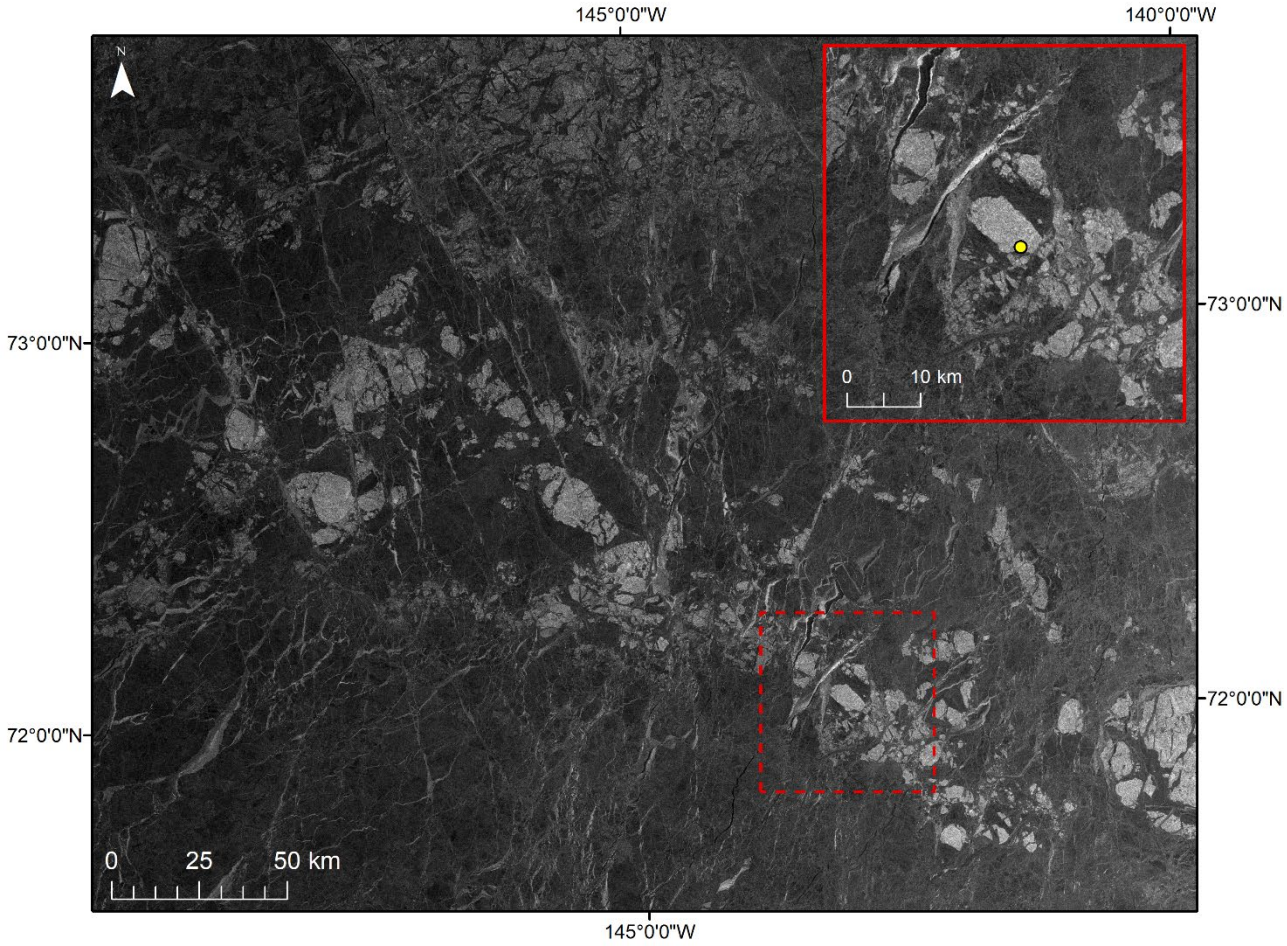

Figure 2. The band of multiyear ice (lighter areas) surrounding the floe chosen for Ice Camp Skate in the Beaufort Sea, as seen from a Sentinel-1 SAR image from 08 March 2018. The inset shows the approximately 50 x 50 km^2 region around the camp (yellow marker).

At the local scale of the camp, snow and ice characteristics within the reflector array were distinctly split between the MYI and FYI (Figure 3). Coincident snow thickness observations and EM31 total-snow-plus-ice thickness observations are used to derive ice thickness. As expected,

the FYI was thinner with a mean ice thickness of 1.0 m and exhibited little variability (SD = 0.2 m), indicating thermodynamic growth and minimal deformation, at least of the pan of ice evaluated. We note that this pan appeared to be a refrozen lead, was selected for a runway and may not be representative of the typical degree of deformation in the area. In contrast, the MYI had a mean ice thickness of 4.3 m and was more spatially variable (SD = 1.3 m) due to mechanical deformation and melt pond formation in prior years. The true mean was greater than this. Approximately 20% of the thickness observations exceeded the 6 m nominal range of the EM31 instrument. The mean snow depth on the FYI and MYI was 13 cm and 43 cm (SD = 10 and 28), respectively, and depth was highly variable over O(10 m) scales on both ice types (Figure 3). Despite being covered with considerably more snow, the upper surface of the MYI was still colder, presumably due to much nearer proximity to seawater of the thinner FYI.

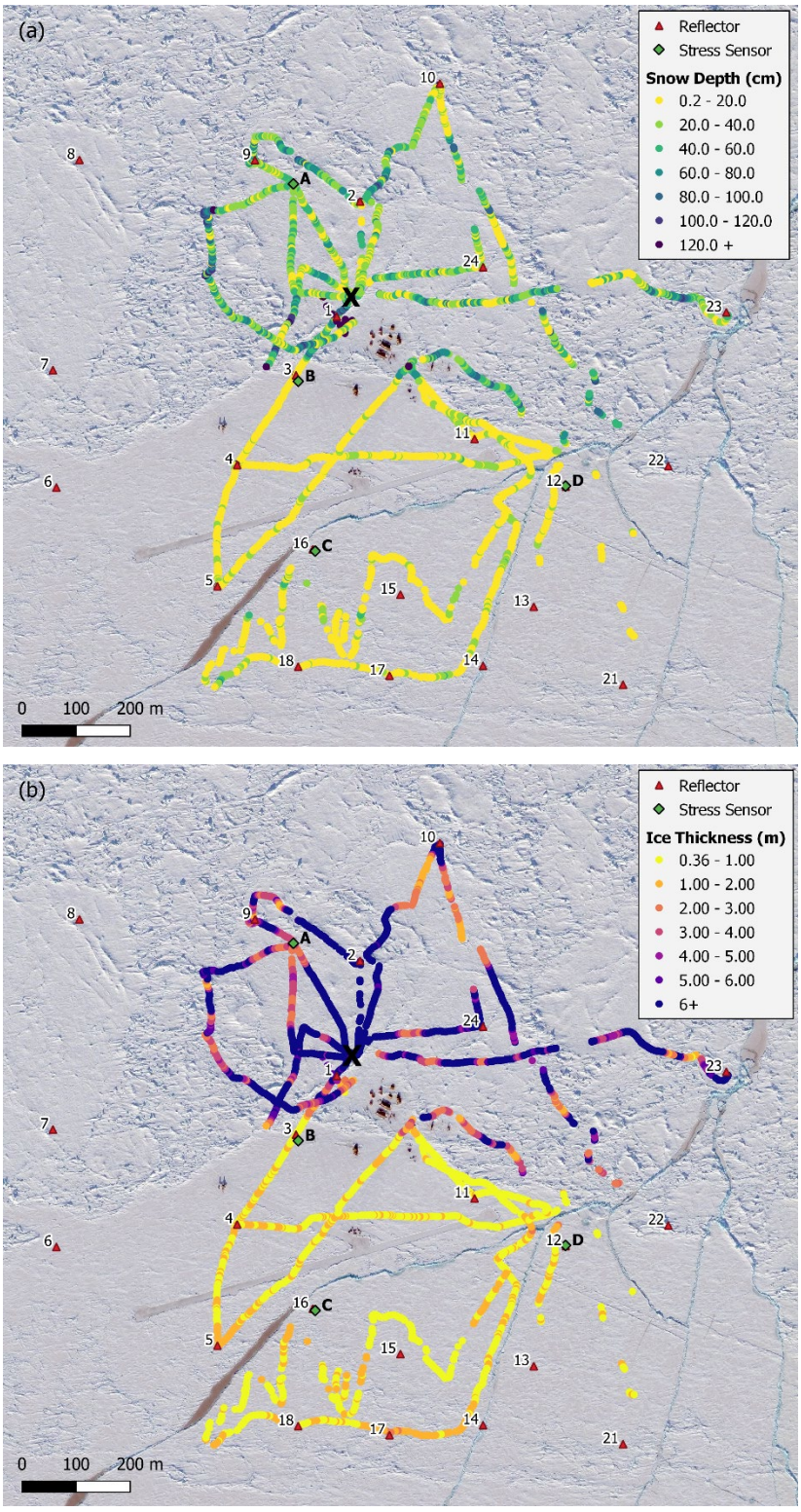

Figure 3. (a) The snow depth (cm) and (b) the ice thickness (m) within the reflector array. Reflectors are depicted as triangles, stress sensors as diamonds, and the laser location indicated with an X. Imagery © 2018, DigitalGlobe, Inc., NextView License.

The predominant wind direction off the north coast of Alaska is influenced by a persistent high pressure system, resulting in an anticyclonic circulation feature called the Beaufort Gyre (Petty et al., 2016; Serreze & Barrett, 2010). The winds are predominantly towards the west, causing westerly large-scale ice drift (Figure 4), and interaction with the northward protruding coastline, all of which was active during our experiment. Ice Camp Skate drifted approximately 160 km westward during the fourteen day study period, from 08-21 March (indicated by the yellow portion of the drift in Figure 4), and the surrounding ice experienced significant deformation resulting in several failure events within the area of our surveys.

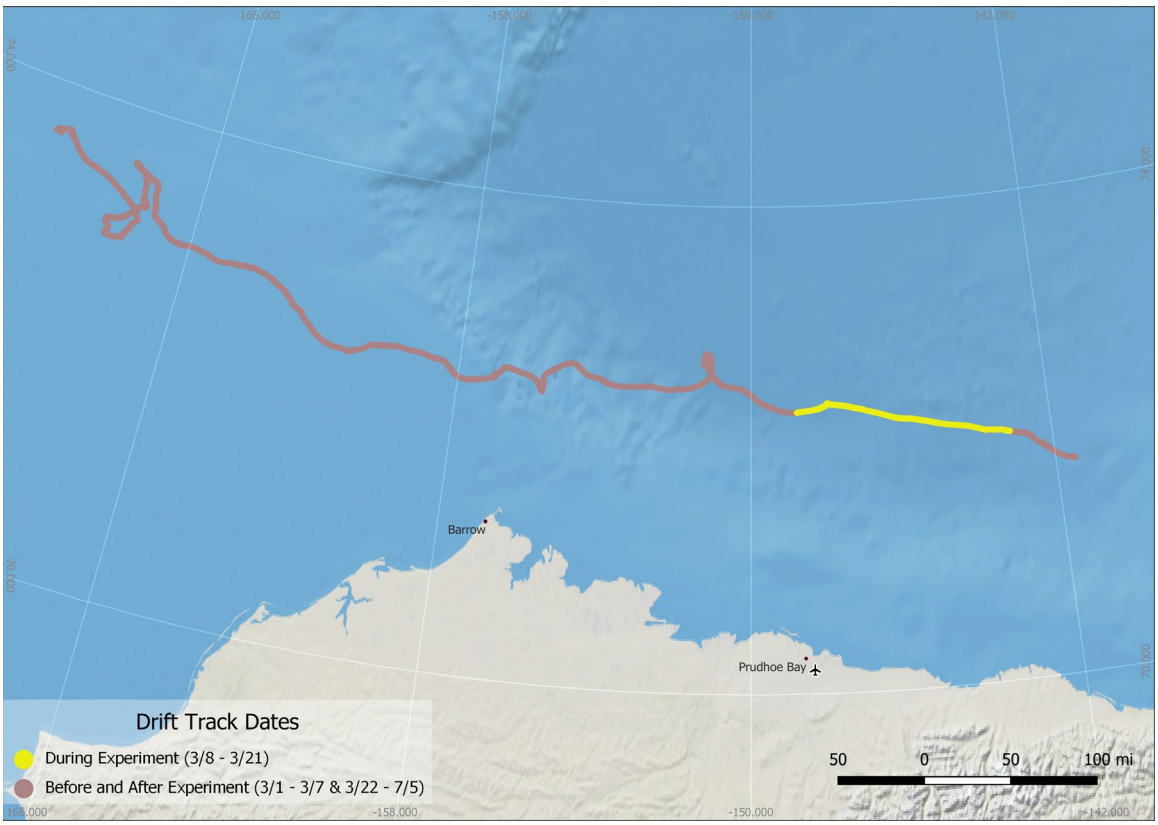

Figure 4. The drift track of the ice camp from 01 March to 05 July 2018. The yellow section denotes the location of the camp during the ICEX experiment, 08 March to 21 March 2018.

3.2 Displacement and Strain Observed Prior to Fracture

The most prominent crack that formed was oriented along a line roughly southwest to northeast across the reflector array and is visible in the 13 March 2018 WorldView image (Figure 1). The crack passed through the original camp runway, interrupting operations and requiring runway relocation. No fracture was noted at the start of the experiment in this location, even along the runway where snow was cleared and close inspections were conducted regularly.

Our first goal is to understand the stress-strain conditions leading up to this failure and, in particular, examine the nature of any advance indications of strains prior to failure. Therefore, in this section we focus on the ice motion well prior to this lead formation event, occurring approximately the first day and a half of the record (08 March 16:00 – 10 March 01:00). During

this time, we believe that the floe components are well-bonded and can be considered monolithic. No evidence of active or recently active flaws was noted. We, therefore, interpret observed displacements within the reflector array as elastic, plastic, or creep deformation of that monolith, using deformation as an indicator of stress state.

The range displacements (i.e. relative change in distance from the total station to the reflector) over time are shown in Figure 5. We found that the TM50 is notably more accurate in repeat ranging than it is at repeat angle determination, with angular determination subject to encoder drift. The greater accuracy of the range observation alone can more clearly show periods when the ice is experiencing strain, and better captures very small disparities in movement between the reflectors (Figure 5).

From 08 March 16:00 to 09 March 08:00, the range displacements are less than 0.5 cm for all reflectors. The ice begins to move more significantly starting 09 March at 8:00 and a notable change in the range displacement of many reflectors is noted until ~16:00 that day. Displacement is continuous over time, indicating non-brittle modes of deformation. The times from this plot inform our selection of time intervals over which to examine the magnitude and direction of net displacement in the reflector array.

In Figure 6, we show total displacement using a visual representation of displacement magnitude and direction based on quiver plots overlain on an optical image of the floe. This presentation illustrates the deformation of the floe intuitively. In Figure 6a, we show displacement during the period from the start of the record 08 March 16:01 to 09 March 08:00. During this time, we see a small net movement of the first year ice reflectors slightly west relative to the MYI floe. This movement is very near the accuracy limits of the technique and consistent with the range-only analysis above; we conclude that little, if any, real deformation is happening during this time. From 08:34 to 16:00 on 09 March, this changes and there is a distinct grouping in displacement of the ice at the reflectors, with displacement values well above detection limits (Figure 6b). Reflectors 4, 5, 13, 14, 15, 16, 17, 18, 20, and 21 are moving approximately southwest relative to the remainder of the reflectors. Reflectors 6 and 7 move southward. The total displacements during this time are less than 2 cm, giving strains of less than 1.5e-5, and strain rates less than 5e-6. These are values within the elastic regime. Unless the ice was heavily pre-loaded, it appears unlikely that yield is reached. Therefore, neither plastic deformation nor brittle failure likely occur during this time. Creep relaxation of some stresses is possible, since strains are not all restored quickly. Calibration of the quasi-static elastic finite element model corroborates this observation. For the displacements in Figure 6b, which span from 09 March at 08:34 to 16:00, a Bayesian p-value of 0.28 was obtained for elastic model. This indicates that there is no strong evidence to reject the elastic model as a description of the ice behavior during this time.

In general, we see the reflectors fall into two groups of deformation. First, we see very limited displacements within the thick MYI. Second, we see relatively larger, coherent movements of the FYI. As we might expect from the accumulation of elastic strain over distance, the reflectors near the FYI/MYI boundary (e.g. 3, 6, 11) exhibit less displacement than those further out on the FYI (e.g. 20, 21). These early indications illustrate that the FYI was, at this time, experiencing significantly greater changes in stress levels than the adjacent MYI.

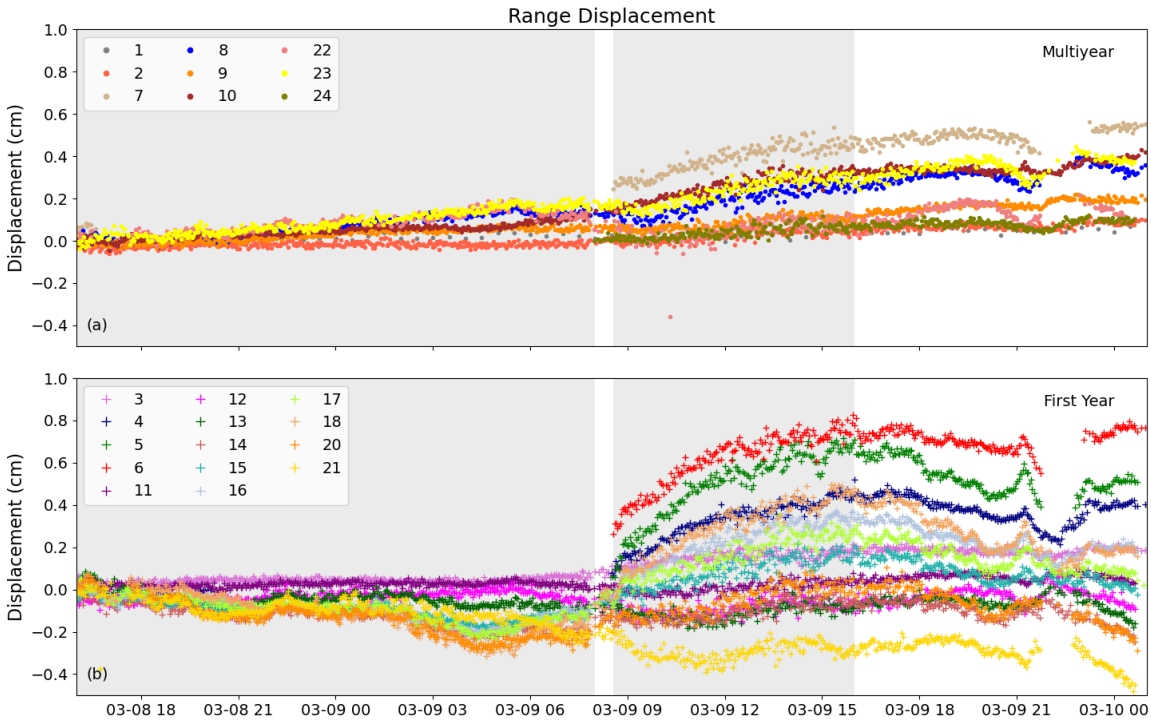

Figure 5. A time series of range displacement (i.e. distance from total station to reflector) at each reflector from 08 March 16:00 to 10 March 01:00, separated into reflectors located on (a) multiyear ice and (b) first year ice. The shaded areas indicate the time periods of interest and the corresponding quiver plots of total displacement are displayed in Figure 6.

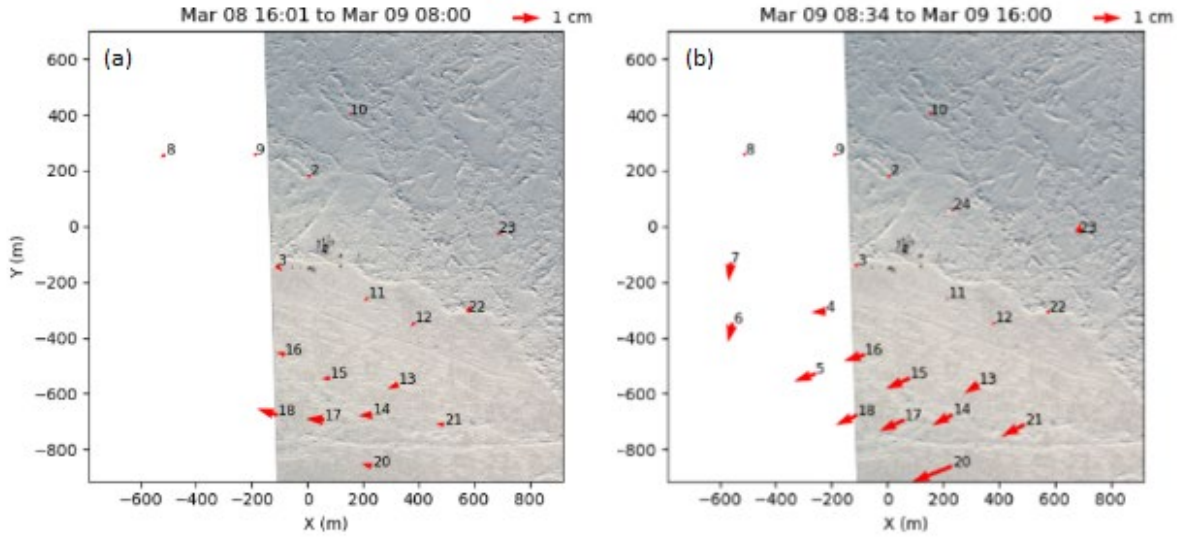

Figure 6. Quiver plots of total displacement at each reflector overlaying WorldView optical imagery of the array from 11 March 2018. The displacements are shown for (a) 08 March 16:01 to 09 March 08:00 and (b) 09 March 08:34 to 09 March 16:00. The plots are referenced to an ice-fixed grid with the total station at (0,0). Imagery © 2018, DigitalGlobe, Inc., NextView License.

3.3 Displacement, strain and stress during the first major fracture event

Due to technical difficulties, the total station did not record data 10 March 2018 01:00 to 12 March 2018 16:45. Vibrating wire stress gage data, which becomes available at this time, provides a way to span this data gap and is critical in determining the fracture timeline (Figure 7). Richter-Menge and Elder (1998) found that changes in the ice temperature are strongly correlated with the secondary principal stress and demonstrated that dynamic stresses, i.e. stress due to external forces, can be estimated by subtracting the secondary principal stress σ_s from the primary principal stress σ_p. In these data, higher stress variability is seen in the FYI than MYI, with particularly high stress variability at first year ice sites B and D, positioned near the FYI-MYI transition. Little transient stress is noted in the MYI, site A. During most of the record, stress change is occurring, but with buildups and releases occurring over many minutes to several hours. A particular example occurs as a larger event starting 11 March at 16:08 and peaking 11 March at 18:53. During the event, compression is indicated at B and D (along the FYI-MYI interface) and varying forces are seen at site C. The stress buildup occurs over hours and then releases relatively gradually over an approximately half an hour period (Figure 7a and b). Due to the magnitude of the stresses and the pattern of their buildup and release, all changes in the early part of this record are indicative of a far-field stress buildup and release, rather than fractures in the immediate study area.

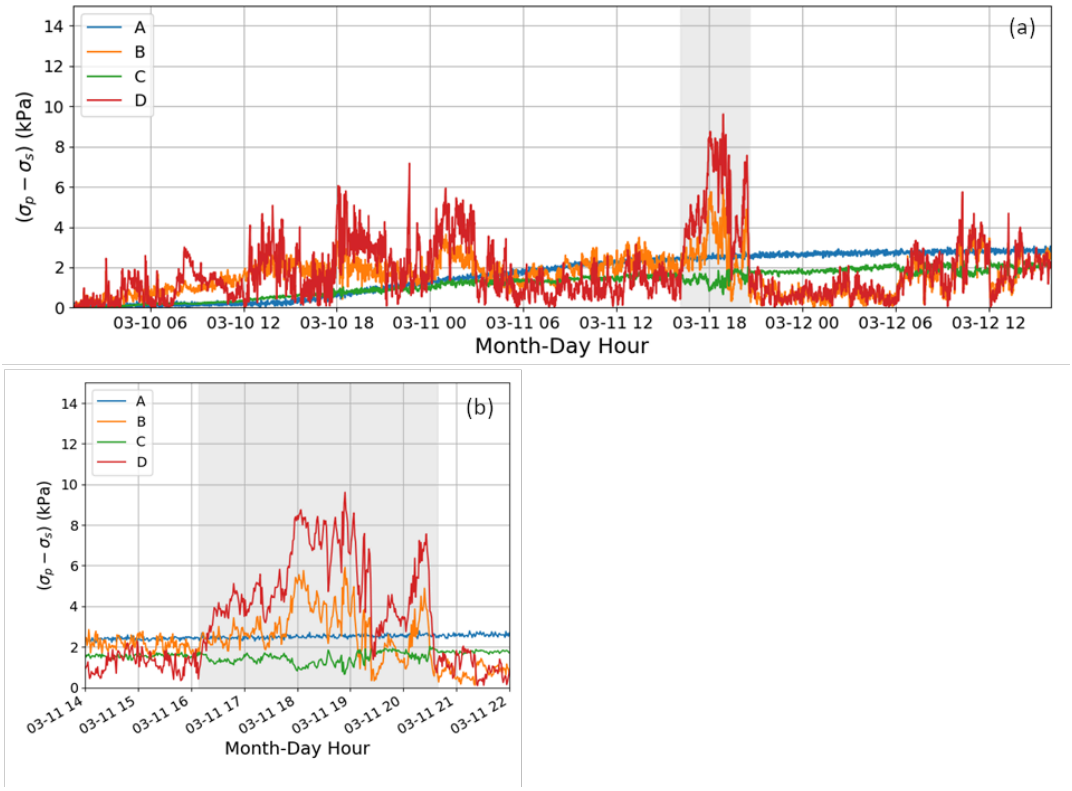

Figure 7. (a) A time series of the dynamic stress (kPa) at each vibrating wire stress gage from 10 March 01:00 to 12 March 16:00. The dynamic stresses are zeroed at the beginning of the time series. The shaded area highlights the event, for which a detailed plot is given in (b) 11 March 16:08 to 11 March 20:40.

A second type of event begins 12 March at 16:30 with a comparatively rapid stress buildup (Figure 8b and d). The stresses peak 12 March at 17:12, with increased dynamic stresses at B, C,

and D, $\Delta(\sigma_p - \sigma_s)$, of 10 kPa, 3 kPa, and 16 kPa, respectively. The stresses then release rapidly to near pre-event levels in less than two minutes (between two successive measurements). The magnitude and rapid release suggest a local fracture. We hypothesize that a portion of the main crack, running roughly southwest to northeast through the array, and noted by personnel on the ice floe later this evening, formed at this time. After this time, the stress sensors on opposite sides of the crack, B and D, appear to be decoupled and no longer demonstrate the similar variability in principal stress that they had prior to this event.

The total station came back online (12 March 16:45), shortly before the stress event indicating a local fracture (12 March 17:12). Therefore, we can examine the fracture event with the benefit of both stress and strain observations. Data covering the period of the fracture event are shown in Figures 8 and 9. Reflector net displacement and gage principal stress are displayed as a time series in Figure 8. Figure 9 provides graphical illustration of the reflector displacements across discrete time windows.

First, the displacement between the last and first full total station observations before and after the data gap (10-12 March) is presented in Figure 9a. These data show substantial compression/convergence occurred from the southeast towards the northwest within the FYI during the interval. Again, consistent with the accumulation of strain over distance, the greatest displacement occurs at those reflectors that are further from the first year/multiyear ice boundary and more distant from the theodolite, with more intervening FYI over which strain can accumulate. The magnitude of this strain approaches, but is less than 1e-4.

Next, we examine stress and strain in a roughly hour-long period of stress accumulation culminating in the initial fracture. Over this time, principal and secondary stresses at B and D become more compressive, with the primary principal stress direction generally aligned northwest to southeast (perpendicular to the crack axis) (Figure 10). Inset plots of stress and reflector displacement (strain proxy) during this time period are shown in Figure 8c and d. An initial buildup of compressive stress at B and D (~16:30-16:49) culminates in a rapid release potentially indicating a primary fracture at 16:49. Associated with this is a smaller magnitude tensile stress buildup at sensor C. The pattern repeats, but with larger compressive stress at B and D from ~16:50-17:11, and a greater spike in tensile stress at sensor C, which is subsequently relieved. Our linear elastic Bayesian analysis also agrees with an initial fracture event occurring during this time period. After calibrating the model to the displacements observed in Figure 9a, a Bayesian p-value of 10^{-3} was found. Unlike the analysis of 09 March, this indicates that the linear elastic model is not a valid description of the ice deformation over this time period, likely because of the fracture event observed in the stress data.

Combined with later imagery and strain data, it appears that under load, a crack formed roughly along a line between stress sensors C and D. A tensile secondary stress at C, is consistent with sliding along the initial crack. It seems likely, based on crack morphology and tensile stress observed at C, that the subsequent extension of the crack to the southwest was behavior characteristic of wing crack formation (Schulson & Hibler, 1991). We support this hypothesis with the strain observations. From 12 March 16:56 to 12 March 17:11, there is minor shearing along the main crack, as seen in Figure 9b, with reflector deformation indicating substantial motion (and, we hypothesize sliding) along the northeastern portion of the reflectors south of the crack, with little deformation to the west where we hypothesize that the crack has not yet formed. When the stress is relieved fully at 17:11, this is accompanied by a quick movement of reflectors 13-21, of about 5 mm (see traces at the top of Figure 9c). Meanwhile, shear movement of

reflectors to the east of the crack, particularly 12, 22, and 23 continues steadily through this time until 17:30, supporting the hypothesis that this portion of the crack had been activated in the event at 16:49 or earlier. The crack does not open significantly immediately after its apparent formation. Total displacement of the reflectors ranges no more than 4 cm, with most reflectors moving less than 1 cm.

It is notable that during this initial fracture event, the relative change in stresses in the ice are small – 21 kPa at peak compression and 3 kPa at peak tension are all that is observed – despite the stress sensors being located very near the actual flaw. Though these relative changes do not represent absolute stress, the background stress in the prior week had been fairly constant. A large, time-invariant stress in a drifting pack would be considered unlikely and so it appears that the ice fractured under relatively low stress, as compared to fracture criteria determined under laboratory settings. We will return to this in our discussion.

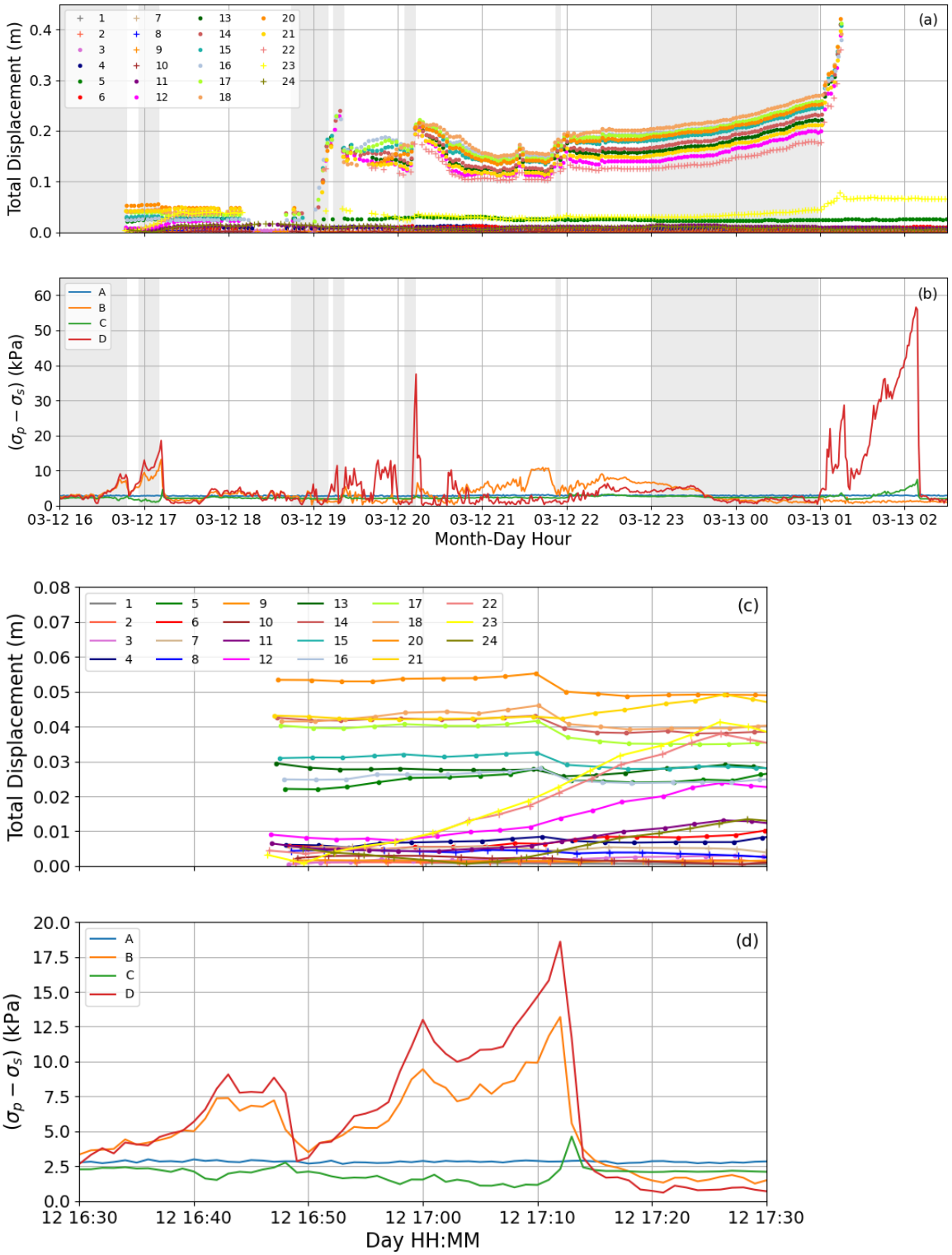

Figure 8. A time series of the (a) total net displacement for each reflector and (b) the dynamic stress recorded at each stress sensor for the time period 12 March 16:00 to 13 March 02:30. The shaded areas correspond to the time periods detailed in the quiver plots in Figure 9. A detailed time series of the event starting 12 March 16:30 is also displayed for total net displacement (c) and dynamic stress (d).

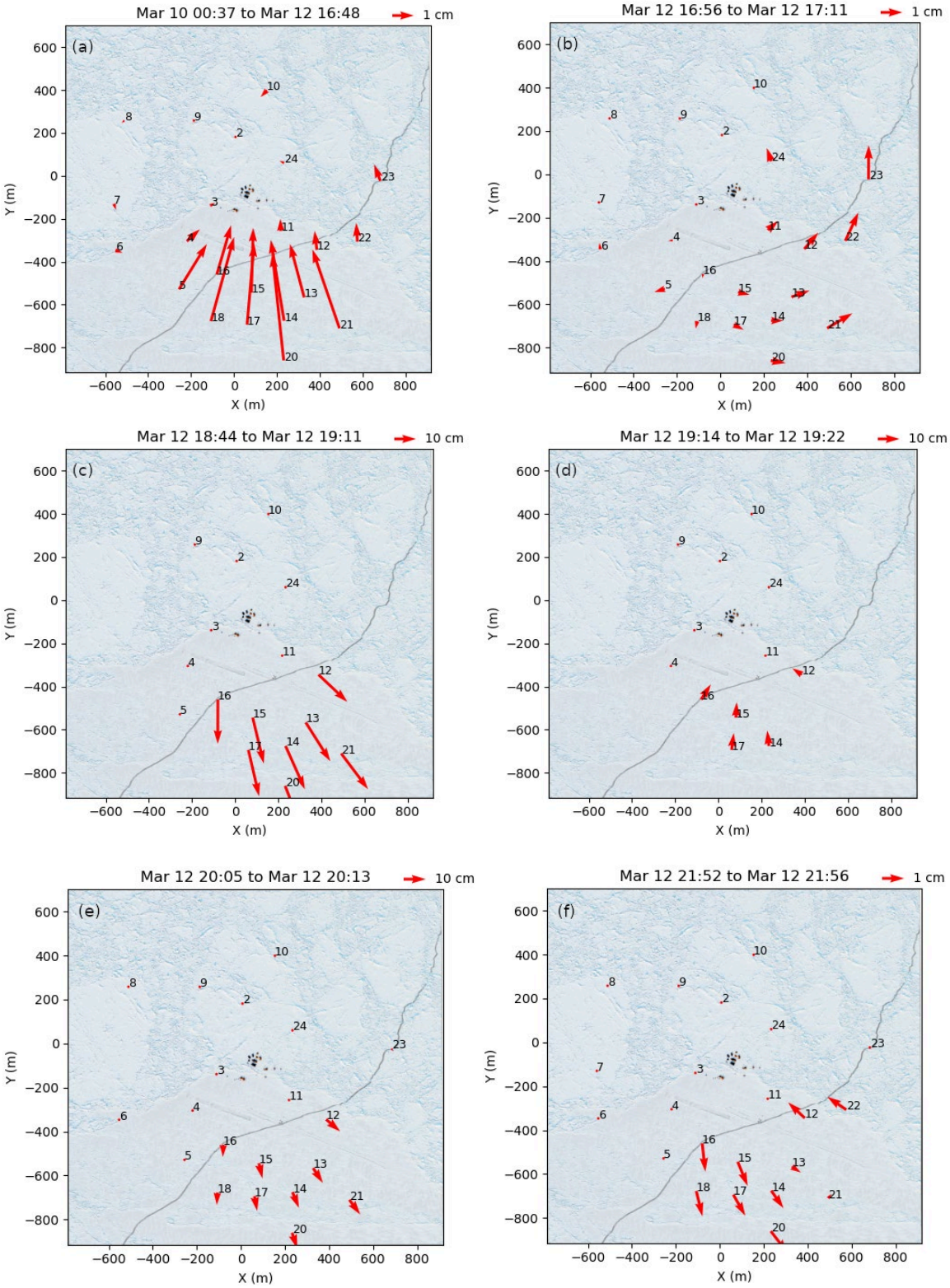
Mar 10 00:37 to Mar 12 16:48
1 cm
(a)
Mar 12 16:56 to Mar 12 17:11
1 cm
(b)
Mar 12 18:44 to Mar 12 19:11
10 cm
(c)
Mar 12 19:14 to Mar 12 19:22
10 cm
(d)
Mar 12 20:05 to Mar 12 20:13
10 cm
(e)
Mar 12 21:52 to Mar 12 21:56
1 cm
(f)
Y (m)
X (m)

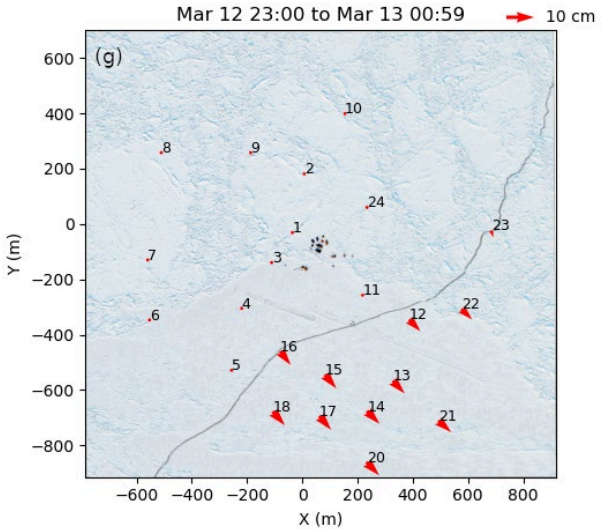

Figure 9. Quiver plot of total displacement at each reflector overlaying WorldView optical imagery of the array from 13 March 2018. The displacements are shown for (a) 10 March 00:37 to 12 March 16:48, (b) 12 March 16:56 to 12 March 17:11, (c) 12 March 18:44 to 12 March 19:11, (d) 12 March 19:14 to 12 March 19:22, (e) 12 March 20:05 to 12 March 20:13, (f) 12 March 21:52 to 12 March 21:56, and (g) 12 March 23:00 to 13 March 00:59. The plots are referenced to an ice-fixed grid with the total station at (0,0). Note that the reference quiver for (a), (b) and (f) represents 1 cm whereas the same for (c), (d), (e), and (g) represents 10 cm. Imagery © 2018, DigitalGlobe, Inc., NextView License.

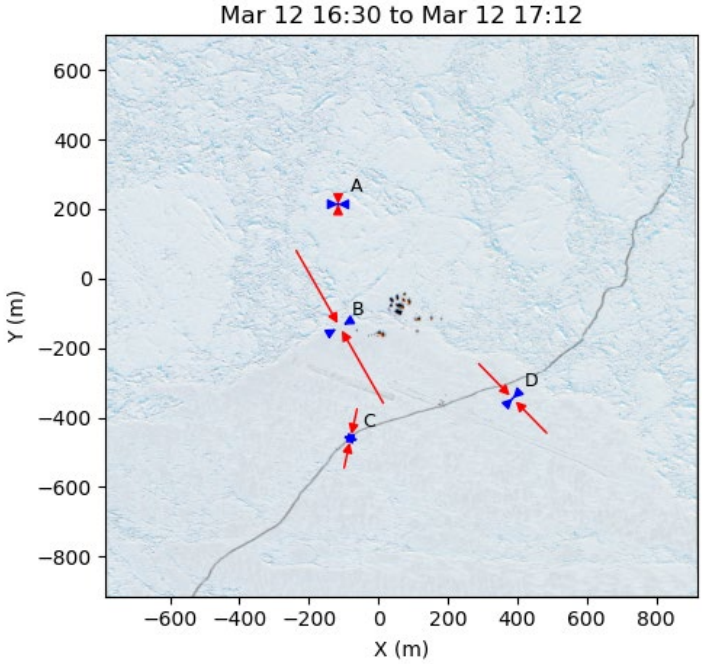

Figure 10. Visualization of the change in stresses between 12 March 16:30 and 12 March 17:12 at each stress sensor overlaying WorldView optical imagery from 13 March 2018. Principal stresses are red and secondary are blue. Arrows pointing inward indicate compression and outward tension. The relative magnitudes are indicated by arrow length. Imagery © 2018, DigitalGlobe, Inc., NextView License.

3.4 Fracture parting and subsequent evolution

Between the fracture event seen at 17:08 until 19:00, little stress is observed on the floe. Displacement observations indicate continued steady shear along the NE portion of the crack from 17:08 until 17:30, but thereafter no measurable strains until 19:00. The main crack then opens abruptly 12 March 19:00. Reflectors to the east of the crack move approximately 15-20 cm toward the southeast (Figure 8 and Figure 9c) in a matter of minutes. Very limited stresses are observed at the time immediately surrounding the crack opening, further supporting our hypothesis that the fracture, in fact, formed several hours earlier, simply waiting for modest forces to permit it to open. Once the rapid initial parting is complete, the lead gradually grows by ~5 cm more over 15 minutes, then abruptly closes by about 5 cm coincident with a spike in compression at stress sensor D (Figures 8 and 9d). We hypothesize that the parted crack began to shear, with the SE portion of the floe moving NE relative to the remainder of the ice. This caused binding on the large protrusion of ice near reflector 12 and stress sensor D at ~19:20. The binding appears to have caused a spike in stress at D until relieved by a fracture/asperity removal. This removal permitted the shearing fracture to close several cm, the reflectors to abruptly displace and the stress at D to drop. Subsequently, over the course of the next few hours (12 March 19:30 to 13 March 00:00), we see further evidence of binding and release near stress sensor D/reflector 12 indicated by abruptly rising and falling stresses at D. Another particularly large event at ~20:13 is characterized by large compression at D, simultaneous to a *parting* of the lead (Figures 8 and 9e). Again, we attribute this to compressive shearing along the crack, but in this case instead of the asperity failing and the lead being permitted to close in compressive shear, the evidence suggests that a secondary crack is opened in the floe to the SE, abruptly relieving the compression near 12 by decoupling the ice there from the body of ice to the SE.

Like the earlier crack we do not see a great deal of motion at the time the fracture appears to have occurred – the primary evidence of it forming is in large stress relief. Subsequently, at times with very little observed stress over the following hours, such as 12 March 21:52 to 21:56, there is, for the first time, evidence of discontinuities in motion on the southeast side of the main crack (Figure 9f). For example, reflectors 12 and 22 are moving opposite the rest of the reflectors on that side of the main flaw 12 March 21:52 to 21:56. Stresses remain steady during this period.

A secondary crack is indeed barely visible in the 13 March 2018 WorldView image. Subsequently, multiple secondary cracks are visible in the 16 and 21 March 2018 Worldview images (Figure 11). The one visible 13 March (challenging to see in 13 March imagery, but easily visible in 21 March imagery) runs between reflectors 12 and 22, and continues southeastward, taking an approximately 90 degree turn at the original runway and runs north-south just east of reflector 21 and the edge of the reflector array. Later images show the intersection of this crack with a network of secondary cracks, many of which may have formed 12-13 March, but not parted sufficiently to be visible in 0.3m resolution imagery taken on the 13 March.

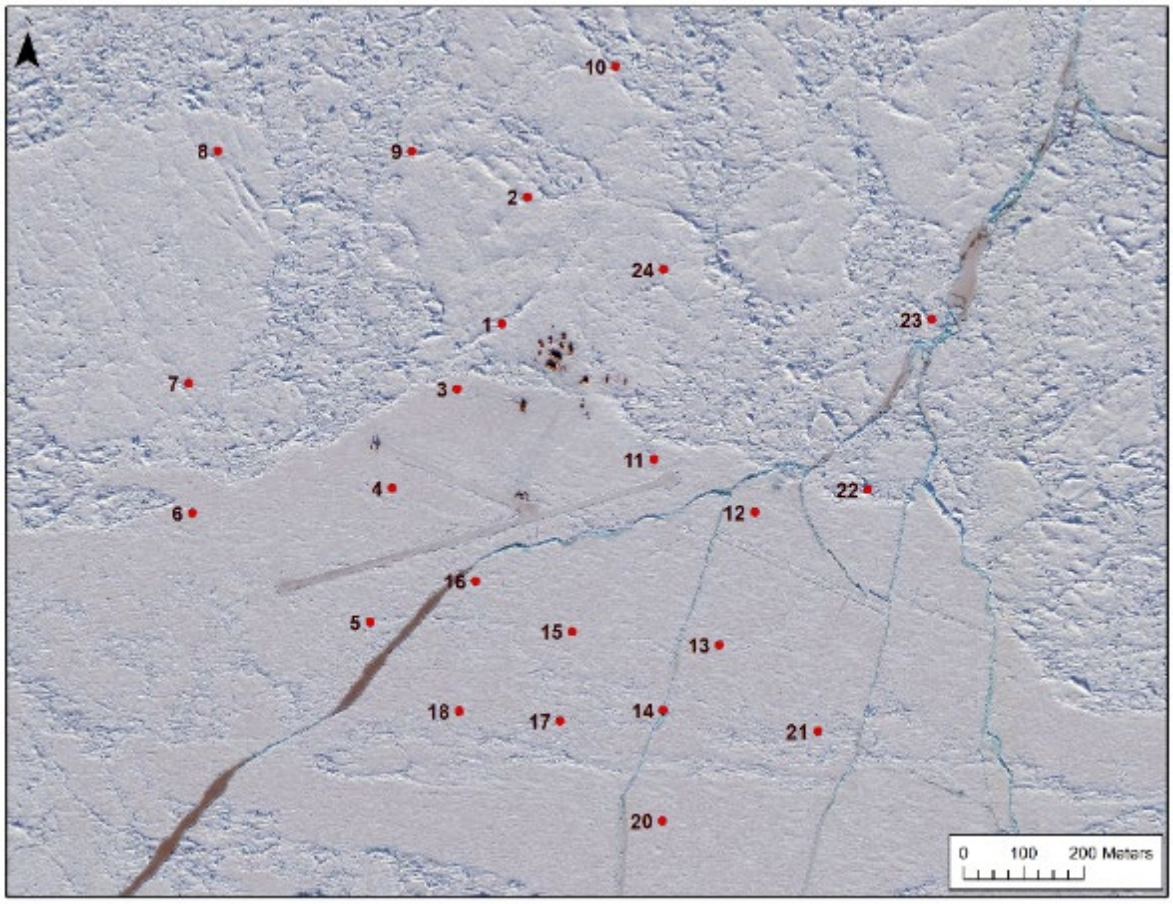

Figure 11. The location of all of the cracks that formed during the experiment as seen on the 21 March WorldView image with the location of the reflectors overlain for reference. Shear along the crack and compressive binding on the sections that protrude (e.g. between reflector 16 and 22) is readily apparent in the image. The team on the ground during this image collection noted ongoing ridge formation near reflector 12. Imagery © 2018, DigitalGlobe, Inc., NextView License.

The continued minor crack divergence and convergences, associated with spikes in stress at D, continue, albeit at lower magnitudes, through about 23:00 as the crack continues to bind, cleave asperities, and drive secondary cracks. After 23:00 and until 13 March 01:00 the crack steadily shears and diverges under minimal local stress, suggesting it has largely cleared the initial binding points and/or that the compressive component of shear has relaxed.

Finally, there is a significant increase in principal stress at sensor D (reflector 12), starting 13 March ~00:00, associated with an onset of a rapid displacement in the laser reflectors (Figure 8 and Figure 12). Shortly after, the reflectors are displaced exponentially as the main crack opens and shears rapidly, and most reflectors move out of their detection windows (Figure 12c). Reflector 22 was displaced approximately 22 m in 2.5 hours. Looking closer at the stress event in Figure 13, we see that the tensile stress is generally aligned with the displacement of the floe to the southeast of the main crack and that there appears to be shearing occurring. The magnitude and release of stress at sensor D, as well as the lack of significant increases at any of the other stress sensors, indicates a local fracture. It is likely that additional secondary fractures occur at this time (13 March 01:08).

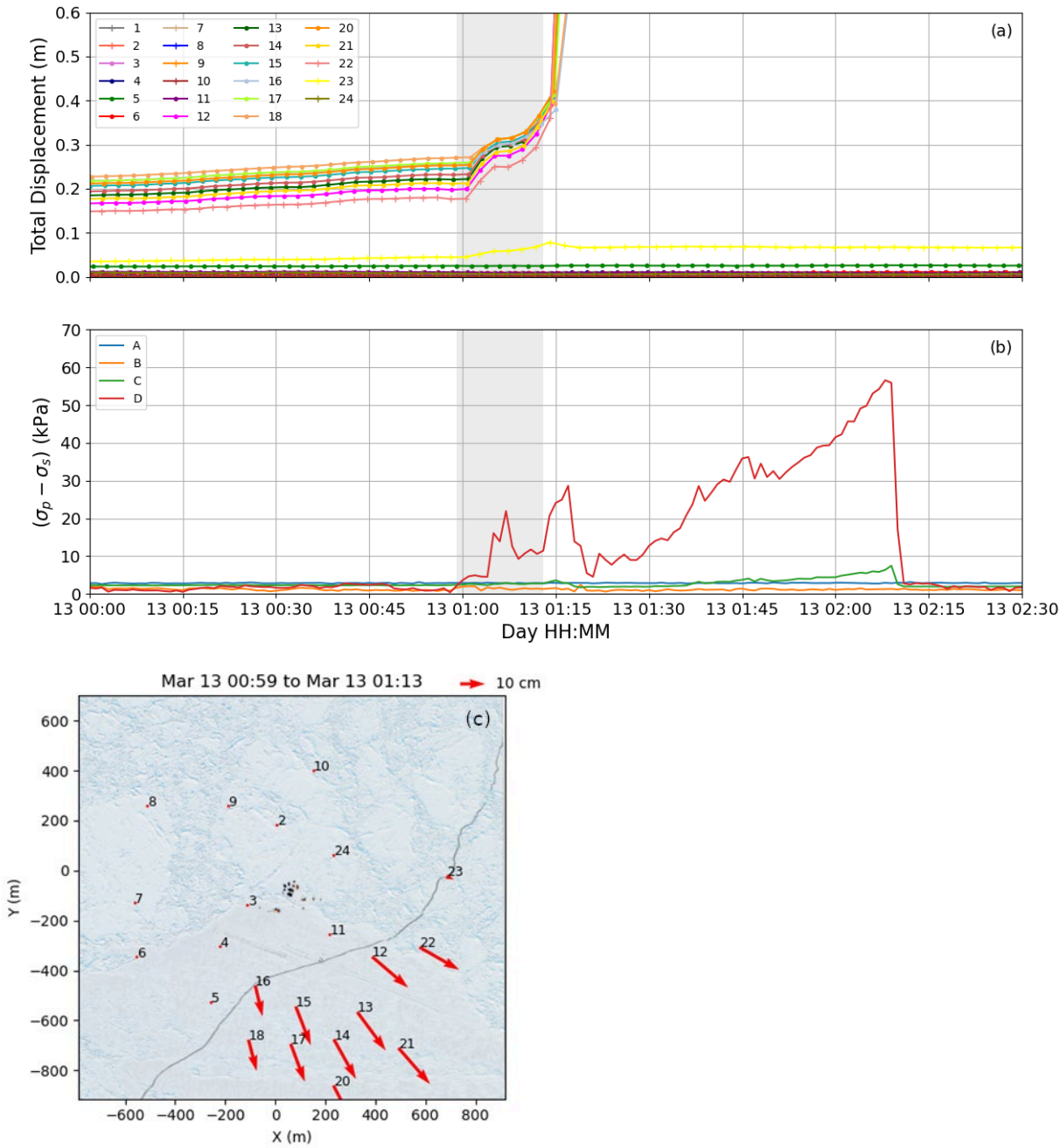

Figure 12. A time series of the (a) total net displacement for each reflector and (b) the dynamic stress recorded at each stress sensor for the time period 13 March 00:00 to 13 March 02:30. (c) Quiver plot of total displacement at each reflector overlaying WorldView optical imagery of the array from 13 March 2018. The displacements are shown for 13 March 00:59 to 13 March 01:13. The plot is referenced to an ice-fixed grid with the total station at (0,0). Imagery © 2018, DigitalGlobe, Inc., NextView License.

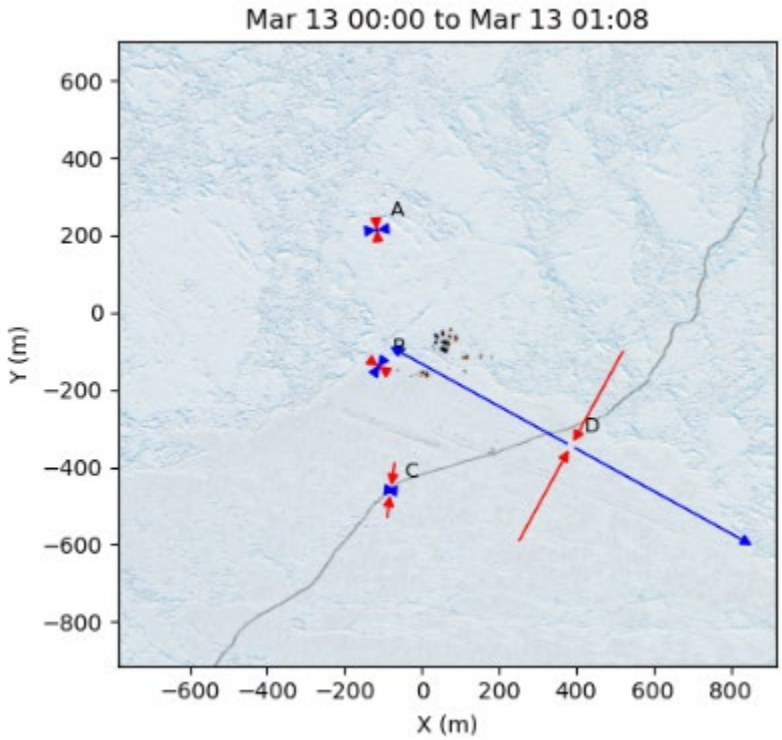

Figure 13. Visualization of the change in stresses between 13 March 00:00 and 13 March 01:08 at each stress sensor. Principal stresses are red and secondary are blue. Arrows pointing inward indicate compression and outward tension (or in this case a reduction in compression). The relative magnitudes are indicated by arrow length. Imagery © 2018, DigitalGlobe, Inc., NextView License.

Further tracking the stress-strain evolution of the floe after this time is impaired by the large displacement of the reflectors to the SE of the crack relative to the observing unit to the NE. These reflectors are lost to detection. We present the rest of the stress record in Figure 14 but limit further discussion. Generally, the initial fracture period is followed by a mostly quiescent period from 13-18 March, punctuated by a period of strong compressive shear that results in ridge building in the fracture from 18-21 March**,** at which point the instruments were retrieved from the ice. The majority of the visible cracks formed to the east of the original crack and in the FYI (Figure 11). Satellite imagery after camp demobilization captures further deformation, which largely destroyed the first year portion of the site in the weeks that followed (Figure 15).

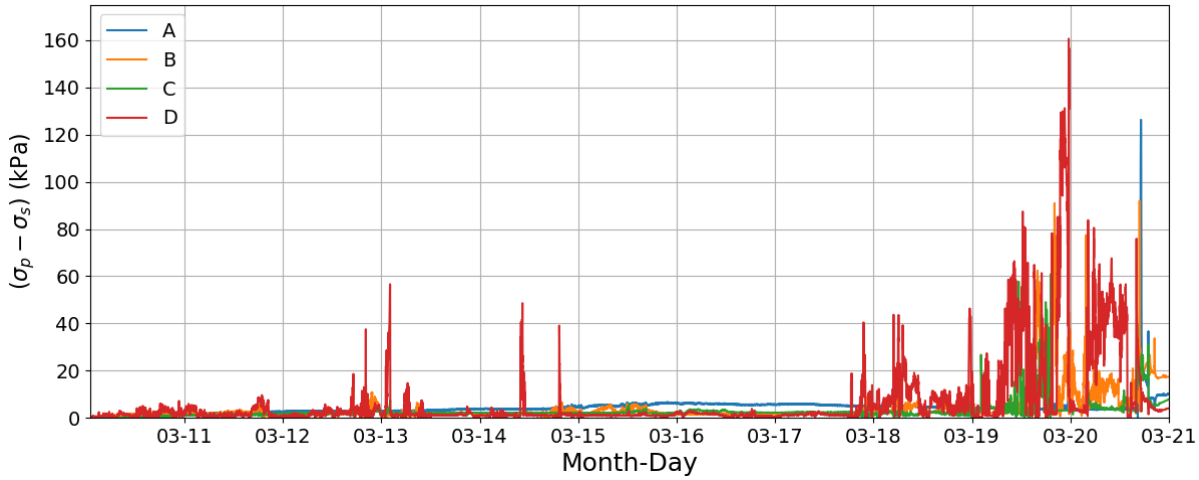

Figure 14. A full time series of the dynamic stress from 10 March to 21 March 2018.

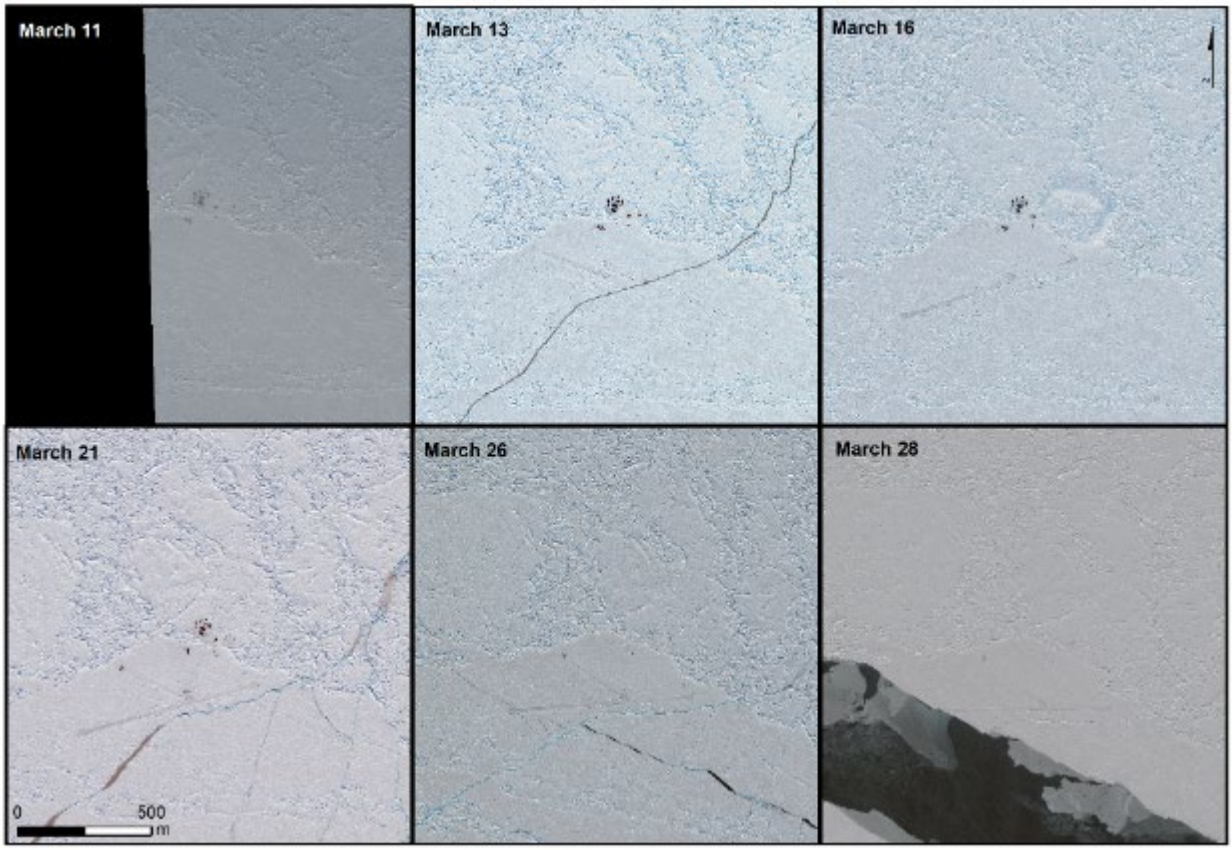

Figure 15. A cropped time series of WorldView optical images centered on Ice Camp Skate chronicling the formation of the initial crack on 13 March 2018 and the subsequent breakup of the surrounding ice. The odd circle of blowing snow in the 16 March image is the result of a helicopter landing. Imagery © 2018, DigitalGlobe, Inc., NextView License.

4 Conclusions

The system deployed here allows, for perhaps the first time, a detailed view of the sea ice dynamics occurring in a deforming ice pack at a fine spatial (cm – 1 km) and temporal (minute) resolution. We capture the formation, elongation, parting, and subsequent shear of a fracture in natural sea ice over a km-scale domain. By carefully evaluating displacement of reflectors and stresses over a period of several days, we gain insight into the modes of action driving the ice failure. A physics-based Bayesian analysis gives us further confidence in our conclusions. Though by themselves these observations are not definitive, available evidence of stress, strain, and fracture modes are found to be consistent with expected modes of failure in compressive shear, including progressive fracture elongation by formation of wing cracks in tensile failure. We further find that after initial fracture, evidence supports several expected modes of flaw zone organization as compressive shear results in the apparent removal of asperities and creation of secondary tensile cracks to accommodate shear. The aggregate of these observations amounts to some of the first direct evidence of these long expected modes of failure acting at scale in a sea ice pack.

The second major finding is an element of predictability in ice failure, highly relevant to on-ice operations. In the case of both the primary and secondary cracks, we observe indications of fracture occurrence in both stress data and strain discontinuities hours prior to the fracture actually parting. In both cases it appears a fracture is created in compressive shear, and that later relaxation permits the crack to open. This finding provides a clear path to detecting flaws in sea ice several hours prior to their likely detection by on-ice personnel or their impact on operations, using the suite of instruments deployed here, at least in some cases. We also noted observable zones of strain concentration within the first year ice at a location similar to, but not exactly aligning with, the location where the future crack formed as much as 4 days in advance (Figure 6b). These strain concentrations may indicate either pre-existing flaws (discontinuities) or simply regions of greater strain under continuous modes of deformation (e.g. elastic strain). Additional effort to explore these types of strain concentration zones with further observations is warranted, but will require a much greater density of stress-strain observations than was available in this dataset. Due to stress coupling, applicability of our linear elastic model, and lack of observed evidence of fractures, even along a cleared runway, we hypothesize that these strain concentrations were not the result of pre-existing flaws. Rather it seems more likely that geometric effects caused by the shape, thickness, and relative modulus of the ice in the area likely result in stress-strain concentration zones. In the future, a similar Bayesian calibration scheme to the one used here could enable more sophisticated models, such as phase-field fracture models or discrete element models, to provide a more detailed characterization of these concentration zones and help identify zones of ice as being at high-risk for fracture.

Our third notable observation is the relatively low stresses observed during the formation of the fracture. The initial formation and elongation of the fracture was associated with relative changes in stress of less than 20 kPa. This is far less than comparable yield criteria observed in laboratory settings (Schulson & Hibler, 1991; Timco & Weeks, 2010). One explanation for this could be that the stress at the flaw location was, in fact, much higher than at the locations that observations were collected. The four stress sensors deployed do demonstrate that stress is highly localized, in agreement with findings by Richter-Menge et al. (2002). However, two of the stress sensors are located within meters of the fracture location, leaving us skeptical that stresses on the

fracture location were greater by orders of magnitude. Well after the flaw has formed, and when it is ridging under strong compressive shear, we do measure larger stresses (i.e. on the order of 100-150 kPa) in ice 60 cm from the actively building ridge. These are consistent with prior observations of stress in natural sea ice, and again are well below failure criteria for sea ice in a laboratory setting. A typical narrative would acknowledge the low far-field stress during fracture in natural sea ice by attributing this discrepancy to force concentration at the fracture tip, and arguing that in a small zone at the fracture tip, the universal yield criteria observed in the laboratory were indeed achieved. Following this argument, the reduced far field stress failure threshold is due to the fact that the stress concentration possible in natural sea ice is much greater than in a laboratory setting, simply because the size of existing flaws is greater. As a compressive shear acts to concentrate stress at the fracture tip, the difference between far field stress and local stress at the fracture tip may in this case be much larger. Given the close proximity of our stress sensors to the propagating fracture tip – C and D were within meters of the flaw and still saw low peak stresses – we find this explanation for the differing stresses observed at laboratory and field scales to be not particularly compelling. Future work with a greater quantity and density of stress sensors and reflectors could further elucidate this discrepancy.

Acknowledgements

We would like to express our deep gratitude to the Arctic Submarine Laboratory for their support in providing logistics to access the drifting pack as part of ICEX Camp Skate. This research was supported through the Office of Naval Research SIDEx program, grant N000142MP001, and as part of the U.S. Army Program Element 060311A, Ground Advanced Technology task for Sensing and Prediction of Arctic Maritime Coastal Conditions. Imagery was provided by the Polar Geospatial Center, National Geospatial Intelligence Agency, and Maxar.

Data Availability Statement

The reflector position and stress sensor data used to derive all of the displacement, strain and stress plots presented in this manuscript are available at Zenodo (https://doi.org/10.5281/zenodo.5076486). Version 1 of the linear elastic finite element model, detailed in the appendix and used to further assess if the ice was behaving in a linear elastic regime or not, is also available as a Python Jupyter Notebook in the same repository.

References

Bouchat, A., & Tremblay, B. (2017). Using sea-ice deformation fields to constrain the mechanical strength parameters of geophysical sea ice. *Journal of Geophysical Research: Oceans*, *122*(7), 5802–5825. https://doi.org/10.1002/2017JC013020

Coon, M. D., Knoke, G. S., Echert, D. C., & Stern, H. L. (1993). Contemporaneous field measurements of pack ice stress and ice strain measurements from SAR imagery. *Proceedings of OCEANS '93*, III31–III36. https://doi.org/10.1109/OCEANS.1993.326154

Cox, G. F., & Johnson, J. B. (1983). *Stress measurements in ice* (CRREL-83-23). Cold Regions Research and Engineering Laboratory.

Dammann, D. O., Eicken, H., Mahoney, A. R., Meyer, F. J., Freymueller, J. T., & Kaufman, A. M. (2018). Evaluating landfast sea ice stress and fracture in support of operations on sea ice using SAR interferometry. *Cold Regions Science and Technology*, *149*, 51–64. https://doi.org/10.1016/j.coldregions.2018.02.001

Dammann, D. O., Johnson, M. A., Fedders, E. R., Mahoney, A. R., Werner, C. L., Polashenski, C. M., Meyer, F. J., & Hutchings, J. K. (2021). Ground-Based Radar Interferometry of Sea Ice. *Remote Sensing*, *13*(1), 43. https://doi.org/10.3390/rs13010043

Damsgaard, A., Adcroft, A., & Sergienko, O. (2018). Application of Discrete Element Methods to Approximate Sea Ice Dynamics. *Journal of Advances in Modeling Earth Systems*, *10*(9), 2228–2244. https://doi.org/10.1029/2018MS001299

Dansereau, V., Weiss, J., Saramito, P., & Lattes, P. (2016). A Maxwell elasto-brittle rheology for sea ice modelling. *The Cryosphere*, *10*(3), 1339–1359. https://doi.org/10.5194/tc-10-1339-2016

Echert, D. C., White, G. B., & Becker, A. (1992). Electromagnetic induction sensing of sea ice thickness using the EM31 ground conductivity meter. *OCEANS 92 Proceedings@m_Mastering the Oceans Through Technology*, *2*, 753–758. https://doi.org/10.1109/OCEANS.1992.607678

Gelman, A., & Shalizi, C. R. (2013). Philosophy and the practice of Bayesian statistics. *British Journal of Mathematical and Statistical Psychology*, *66*(1), 8–38.

Hata, Y., & Tremblay, L. B. (2015). Anisotropic internal thermal stress in sea ice from the Canadian Arctic Archipelago. *Journal of Geophysical Research: Oceans*, *120*(8), 5457–5472. https://doi.org/10.1002/2015JC010819

Herman, A. (2016). Discrete-Element bonded-particle Sea Ice model DESIgn, version 1.3a – model description and implementation. *Geoscientific Model Development*, *9*(3), 1219–1241. https://doi.org/10.5194/gmd-9-1219-2016

Hopkins, M. A. (2004). A discrete element Lagrangian sea ice model. *Engineering Computations*, *21*(2/3/4), 409–421. https://doi.org/10.1108/02644400410519857

Hutchings, J. K., Geiger, C. A., Roberts, A., Richter-Menge, J. A., & Elder, B. (2010). *On the Spatial and Temporal Characterization of Motion Induced Sea Ice Internal Stress*. International Conference and Exhibition on Performance of Ships and Structures in Ice.

Hutchings, J. K., & Hibler, W. D. (2008). Small-scale sea ice deformation in the Beaufort Sea seasonal ice zone. *Journal of Geophysical Research: Oceans*, *113*(C8). https://doi.org/10.1029/2006JC003971

Inoue, J. (2020). Review of forecast skills for weather and sea ice in supporting Arctic navigation. *Polar Science*, 100523. https://doi.org/10.1016/j.polar.2020.100523

Itkin, P., Spreen, G., Cheng, B., Doble, M., Girard-Ardhuin, F., Haapala, J., Hughes, N., Kaleschke, L., Nicolaus, M., & Wilkinson, J. (2017). Thin ice and storms: Sea ice deformation from buoy arrays deployed during N-ICE2015. *Journal of Geophysical Research: Oceans*, *122*(6), 4661–4674. https://doi.org/10.1002/2016JC012403

Johnson, J. B. (1985). In-Ice Calibration Tests for an Elongated, Uniaxial Brass Ice Stress Sensor. *Journal of Energy Resources Technology*, *107*(4), 506–510. https://doi.org/10.1115/1.3231226

Jones, J., Eicken, H., Mahoney, A., Mv, R., Kambhamettu, C., Fukamachi, Y., Ohshima, K. I., & George, J. C. (2016). Landfast sea ice breakouts: Stabilizing ice features, oceanic and atmospheric forcing at Barrow, Alaska. *Continental Shelf Research*, *126*, 50–63. https://doi.org/10.1016/j.csr.2016.07.015

Kovacs, A., & Morey, R. M. (1991). *Evaluation of a Portable Electromagnetic Induction Instrument for Measuring Sea Ice Thickness* (CRREL Report 91-12; p. 24). Cold Regions Research and Engineering Laboratory.

Kruschke, J. K. (2013). Posterior predictive checks can and should be Bayesian: Comment on Gelman and Shalizi,'Philosophy and the practice of Bayesian statistics.' *British Journal of Mathematical and Statistical Psychology*, *66*(1), 45–56.

Kurtz, N. T., Markus, T., Farrell, S. L., Worthen, D. L., & Boisvert, L. N. (2011). Observations of recent Arctic sea ice volume loss and its impact on ocean-atmosphere energy exchange and ice production. *Journal of Geophysical Research: Oceans*, *116*(C4). https://doi.org/10.1029/2010JC006235

Kwok, R., Hunke, E. C., Maslowski, W., Menemenlis, D., & Zhang, J. (2008). Variability of sea ice simulations assessed with RGPS kinematics. *Journal of Geophysical Research*, *113*(C11), C11012. https://doi.org/10.1029/2008JC004783

Lewis, B. J., & Hutchings, J. K. (2019). Leads and Associated Sea Ice Drift in the Beaufort Sea in Winter. *Journal of Geophysical Research: Oceans*, *124*(5), 3411–3427. https://doi.org/10.1029/2018JC014898

Lewis, J. K., & Richter-Menge, J. A. (1998). Motion-induced stresses in pack ice. *Journal of Geophysical Research: Oceans*, *103*(C10), 21831–21843.

Li, S., Shapiro, L., McNutt, L., & Feffers, A. (1996). Application of Satellite Radar Interferometry to the Detection of Sea Ice Deformation. *Journal of the Remote Sensing Society of Japan*, *16*(2), 153–163. https://doi.org/10.11440/rssj1981.16.153

Lindsay, R. W., Zhang, J., & Rothrock, D. A. (2003). Sea-ice deformation rates from satellite measurements and in a model. *Atmosphere-Ocean*, *41*(1), 35–47. https://doi.org/10.3137/ao.410103

Logg, A., Mardal, K.-A., & Wells, G. (2012). *Automated solution of differential equations by the finite element method: The FEniCS book* (Vol. 84). Springer Science & Business Media.

Lund, B., Graber, H. C., Persson, P. O. G., Smith, M., Doble, M., Thomson, J., & Wadhams, P. (2018). Arctic Sea Ice Drift Measured by Shipboard Marine Radar. *Journal of Geophysical Research: Oceans*, *123*(6), 4298–4321. https://doi.org/10.1029/2018JC013769

Mahoney, A. R., Dammann, D. O., Johnson, M. A., Eicken, H., & Meyer, F. J. (2016). Measurement and imaging of infragravity waves in sea ice using InSAR. *Geophysical Research Letters*, *43*(12), 6383–6392. https://doi.org/10.1002/2016GL069583

Marsan, D., Stern, H., Lindsay, R., & Weiss, J. (2004). Scale Dependence and Localization of the Deformation of Arctic Sea Ice. *Physical Review Letters*, *93*(17), 178501. https://doi.org/10.1103/PhysRevLett.93.178501

Oikkonen, A., Haapala, J., Lensu, M., & Karvonen, J. (2016). Sea ice drift and deformation in the coastal boundary zone. *Geophysical Research Letters*, *43*(19), 10,303-10,310. https://doi.org/10.1002/2016GL069632

Petty, A. A., Hutchings, J. K., Richter-Menge, J. A., & Tschudi, M. A. (2016). Sea ice circulation around the Beaufort Gyre: The changing role of wind forcing and the sea ice state. *Journal of Geophysical Research: Oceans*, *121*(5), 3278–3296. https://doi.org/10.1002/2015JC010903

Rampal, P., Weiss, J., Marsan, D., Lindsay, R., & Stern, H. (2008). Scaling properties of sea ice deformation from buoy dispersion analysis. *Journal of Geophysical Research*, *113*(C3), C03002. https://doi.org/10.1029/2007JC004143

Rasmussen, C. E. (2003). Gaussian processes in machine learning. *Summer School on Machine Learning*, 63–71.

Richter-Menge, J. A., & Elder, B. C. (1998). Characteristics of pack ice stress in the Alaskan Beaufort Sea. *Journal of Geophysical Research: Oceans*, *103*(C10), 21817–21829. https://doi.org/10.1029/98JC01261

Richter-Menge, J. A., McNutt, S. L., Overland, J. E., & Kwok, R. (2002). Relating arctic pack ice stress and deformation under winter conditions. *Journal of Geophysical Research*, *107*(C10), 8040. https://doi.org/10.1029/2000JC000477

Schulson, E. M., & Duval, P. (2009). *Creep and Fracture of Ice*. Cambridge University Press. https://hal-insu.archives-ouvertes.fr/insu-00421610

Schulson, E. M., & Hibler, W. D. (1991). The fracture of ice on scales large and small: Arctic leads and wing cracks. *Journal of Glaciology*, 4.

Serreze, M. C., & Barrett, A. P. (2010). Characteristics of the Beaufort Sea High. *Journal of Climate*, *24*(1), 159–182. https://doi.org/10.1175/2010JCLI3636.1

Spreen, G., Kwok, R., Menemenlis, D., & Nguyen, A. T. (2017). Sea-ice deformation in a coupled ocean–sea-ice model and in satellite remote sensing data. *The Cryosphere*, *11*(4), 1553–1573. https://doi.org/10.5194/tc-11-1553-2017

Stroeve, J., & Notz, D. (2018). Changing state of Arctic sea ice across all seasons. *Environmental Research Letters*, *13*(10), 103001. https://doi.org/10.1088/1748-9326/aade56

Sturm, M., & Holmgren, J. (2017). An Automatic Snow Depth Probe for Field Validation Campaigns. *Water Resources Research*, 9695–9701. https://doi.org/10.1029/2018WR023559@10.1002/(ISSN)1944-7973.SNOWEX1

Templeton, J. S. (1980). Measurement of sea ice pressures. *POAC 79, Proceedings of the 5th International Conference on Port and Ocean Engineering under Arctic Conditions*, *1*, 73–78.

Thorndike, A. S., Rothrock, D. A., Maykut, G. A., & Colony, R. (1975). The thickness distribution of sea ice. *Journal of Geophysical Research (1896-1977)*, *80*(33), 4501–4513. https://doi.org/10.1029/JC080i033p04501

Timco, G. W., & Weeks, W. F. (2010). A review of the engineering properties of sea ice. *Cold Regions Science and Technology*, *60*(2), 107–129. https://doi.org/10.1016/j.coldregions.2009.10.003

Tucker, W. B., & Perovich, D. K. (1992). Stress measurements in drifting pack ice. *Cold Regions Science and Technology*, *20*(2), 119–139. https://doi.org/10.1016/0165-232X(92)90012-J

Weiss, J. (2013). *Drift, Deformation, and Fracture of Sea Ice*. Springer Netherlands. https://doi.org/10.1007/978-94-007-6202-2

Weiss, J., Schulson, E. M., & Stern, H. L. (2007). Sea ice rheology from in-situ, satellite and laboratory observations: Fracture and friction. *Earth and Planetary Science Letters*, *255*(1), 1–8. https://doi.org/10.1016/j.epsl.2006.11.033

Wilchinsky, A. V., Feltham, D. L., & Hopkins, M. A. (2011). Modelling the reorientation of sea-ice faults as the wind changes direction. *Annals of Glaciology*, *52*(57), 83–90. https://doi.org/10.3189/172756411795931831

Xie, T., Perrie, W., Fang, H., Zhao, L., Yu, W., & He, Y. (2017). Spatial and temporal variability of sea ice deformation rates in the Arctic Ocean observed by RADARSAT-1. *Science China Earth Sciences*, *60*(5), 858–865. https://doi.org/10.1007/s11430-017-9023-8

A Bayesian Model Calibration and p-Values

We employed a quasi-static linear elastic model to help determine the timing of fracture events in our data. During times when this model can accurately capture the observed ice behavior, it is unlikely that fracture events or other nonlinear mechanical behavior has occurred. Here we provide the mathematical details of our model, its calibration to the observation data, and the use of calibration results for statistically assessing how well the model captures the observational data using a Bayesian generalization of classic p-value tests.

A.1 Linear Elastic Model

Here our goal is not to develop a model that can capture the ice behavior under different breakup scenarios, but to construct a continuum mechanics model that could accurately capture elastic deformation of the ice. If the elastic model cannot reasonably capture the observed ice deformation, the ice is likely not in an elastic regime and some sort of fracture has likely occurred. A quantitative process for verifying elastic behavior is provided below.
To start, we ignore inertial effects and adopt a quasi-static description of the ice. We further assume that the ice is a continuum with stresses propagating horizontally through the ice. This allows us to adopt a plane-stress formulation. Assuming isotropic (but possibly heterogeneous) material properties, the strain-stress relationship is completely defined by the Lame parameters λ, μ and Hooke's law. Combined with the common assumption of small strain and the balance of momentum, we obtain the following linear-elastic system

$$-\nabla \cdot \big(h(x)\sigma(x)\big) = 0 \ \ on\ \Omega \tag{1}$$

$$\sigma(x) = 2\mu\varepsilon(x) + \lambda tr\big(\varepsilon(x)\big)I\ on\ \Omega \tag{2}$$

$$\varepsilon(x) = \frac{1}{2}(\nabla u + \nabla u^T)\ on\ \Omega \tag{3}$$

$$u(x) = u_{bc}(x)\ on\ \partial\Omega \tag{4}$$

$$u(x) = 0 \ \ at\ (0,0) \tag{5}$$

where Ω is the model domain, $\partial\Omega$ is the domain boundary, $h(x)$ is the ice thickness, and $u_{bc}(x)$ represents Dirichlet boundary conditions. The zero displacement condition at $(0,0)$ captures the fact that we are using an ice-fixed reference frame with the laser always at the origin. Note that we have also ignored body forces in the balance of momentum. For sea ice, body forces like atmospheric drag act over very large areas. For small model domains, like Ω, there is insufficient area for these body forces to accumulate substantially. Wind and ocean currents thus influence the modeled displacement $u(x)$ through the Dirichlet boundary conditions $u_{bc}(x)$ on the model domain $\partial\Omega$.

The ice thickness $h(x)$ is set to 4m over the multiyear ice and 1m for first year ice. The MYI-FYI boundary is delineated with a piecewise linear boundary through manual inspection of optical imagery.

To solve the system in (1) – (5) and evaluate the modeled displacement field $u(x)$ at the reflector locations, we employ a finite element discretization using the Fenics package (Logg et al., 2012). Let $\hat{u}_{bc}$ denote a vector of boundary displacement degrees of freedom in the finite element discretization and let $\hat{u}_{pred}$ denote a vector of model displacements at the reflector positions. The finite element discretization allows us to construct an observation matrix *B* and a stiffness matrix *K* such that

$$\hat{u}_{pred} = BK^{-1}\hat{u}_{bc} \tag{6}$$

A.2 Bayesian Calibration

The vector of boundary displacement $\hat{u}_{bc}$ in (6) cannot be observed directly and must be calibrated so that the model predictions agree with observational data. Notice that there are many more boundary degrees of freedom in the finite element discretization than the number of reflectors (and thus the number of displacement observations). The calibration problem is therefore ill-posed: there are many possible boundary conditions that will match the displacement observations equally well. We adopt a Bayesian approach to probabilistically account for the uncertainty caused by this ill-posedness. Using a Bayesian framework also allows us to account for observation noise in the data and incorporate additional assumptions on the boundary conditions (smoothness, magnitudes, etc.).

We are interested in a probability distribution $p(\hat{u}_{bc}|\hat{u}_{obs})$, where $\hat{u}_{obs}$ is a vector of displacement observations at the reflectors. Bayes' rule expands this distribution into a prior distribution $p(\hat{u}_{bc})$ and a likelihood function $p(\hat{u}_{obs}|\hat{u}_{bc})$, such that

$$p(\hat{u}_{bc}|\hat{u}_{obs}) \propto p(\hat{u}_{obs}|\hat{u}_{bc})p(\hat{u}_{bc}) \tag{7}$$

The likelihood function incorporates the finite element as well as a statistical description of the observation error. We assume an additive Gaussian error model of the form $\hat{u}_{obs} = \hat{u}_{ref} + \epsilon$, where $\epsilon \sim N(0, \Sigma_\epsilon)$ is a Gaussian random variable with covariance Σ. Features of the laser observing system are used to derive this covariance. The laser observing system has different noise levels in radial and tangential direction (relative to the laser position at $(0,0)$). The reported error in the range (radial direction) is 0.6mm +1mm/km. The reported error in the angular measurement is 1.4 x 10^{-4} degrees. Let r be the range measurement with standard deviation σ_r and let θ be the angular measurement with standard deviation σ_θ. These are related to the Cartesian coordinates (x, y) through

$$\begin{bmatrix} x \\ y \end{bmatrix} = \begin{bmatrix} r\cos\theta \\ r\sin\theta \end{bmatrix}$$

We now turn to propagating errors in the range and angle into correlated errors in the Cartesian coordinates. We assume the observed range is given by $r_{obs} = \bar{r} + (\sigma_r + \alpha_r\bar{r})z_r$, where $\bar{r}$ is the true range and z_r is a standard normal random variable. Using the manufacturer-reported errors, the values of σ_r and α_r would be 0.6mm and 1mm/km, respectively. The observed angle is similarly defined, but without the multiplicative term: $\theta_{obs} = \bar{\theta} + \sigma_\theta z_\theta$. Using these definitions, the observed Cartesian coordinates are given by

$$\begin{bmatrix} x_{obs} \\ y_{obs} \end{bmatrix} = \begin{bmatrix} \bar{r} + (\sigma_r + \alpha_r \bar{r}) z_r) \cos(\bar{\theta} + \sigma_\theta z_\theta) \\ \bar{r} + (\sigma_r + \alpha_r \bar{r}) z_r) \sin(\bar{\theta} + \sigma_\theta z_\theta) \end{bmatrix}$$

The mapping from (z_r, z_θ) to (x_{obs}, y_{obs}) is nonlinear and the joint distribution of the Cartesian coordinates (x_{obs}, y_{obs}) is therefore non-Gaussian. To simplify computation, we will instead use a Gaussian approximation based on a linear approximation of the $(z_r, z_\theta) \rightarrow (x_{obs}, y_{obs})$ mapping. The Jacobian of the transformation with respect to (z_r, z_θ) evaluated at $(0,0)$ is given by

$$J = \begin{bmatrix} (\sigma_r + \alpha_r \bar{r}) \cos(\bar{\theta}) & -\sigma_\theta \bar{r} \sin(\bar{\theta}) \\ (\sigma_r + \alpha_r \bar{r}) \sin(\bar{\theta}) & \sigma_\theta \bar{r} \cos(\bar{\theta}) \end{bmatrix}$$

This Jacobian matrix defines the covariance between the Cartesian components of an observation of a single reflector's position. Since the displacement is given by the difference of two position measurements, the covariance of the displacement at a single reflector is given by

$$\Sigma_{ref} = 2JJ^T$$

This covariance can be computed for each reflector and used to define the covariance of the additive noise Σ_ϵ.

Notice that the Jacobian J depends on the mean range $\bar{r}$, which is our model output. This multiplicative term would result in a non-Gaussian posterior distribution that cannot be characterized analytically. To leverage efficient Gaussian calculations, we will again make an additional approximation and use the observed range to define the covariance Σ so that Σ does not depend on the unknown true range $\bar{r}$.

For the prior distribution over the boundary degrees of freedom $p(\hat{u}_{bc})$, we view $\hat{u}_{bc}$ as the discretization of a zero-mean Gaussian process such that $p(\hat{u}_{bc}) = N(0, \Sigma_u)$. To account for larger displacements farther from the origin, we employ a nonstationary modification of the standard squared exponential kernel. The horizontal and vertical components of the boundary displacements are treated as independent identically distributed random variables with the same covariance kernel. The nonstationary kernel takes the form

$$k(x, x') = \sigma_u(x)\sigma_u(x') exp\left[-\frac{\|x - x'\|^2}{L^2}\right] \quad (8)$$

where $\sigma_u(x) = \bar{\sigma}_u \|x\|$ is a position-dependent standard deviation. For FYI, we assume a failure strain of 2 x 10^{-4} and set $\bar{\sigma}_u = 10^{-4}$ so that the failure strain is at approximately the 95% quantile. For the thicker MYI, we assume a failure strain of 4 x 10^{-5} and set $\bar{\sigma}_u = 2\ x\ 10^{-5}$. We further assume that there is no prior correlation between boundary conditions on MYI and FYI. The length scale was set to $L = 100$ meters. Note that the linear-elastic model used here does not account for creep, plastic deformation, or strain-rate dependencies. However, we are not trying to develop a high-fidelity model of ice mechanics that might account for such processes; our goal is to quantitatively assess if the ice is in the linear-elastic regime. If the model can capture the observed behavior with "reasonable" boundary conditions then it is likely in the linear-elastic regime. The failure strains and correlation lengths used to define the covariance kernel $k(x, x')$, are a statistical way of defining what "reasonable" means.

Using the linear model in (6) with Σ_ϵ and Σ_u results in a linear-Gaussian Bayesian inference problem that can be solved analytically to obtain a Gaussian posterior over the boundary displacements $\hat{u}_{bc}$ with mean μ_{post} and covariance Σ_{post}. See (Rasmussen, 2003) for details. The posterior mean μ_{post} provides a "best" estimate of the boundary displacements while Σ_{post} describes uncertainty in those boundary conditions stemming from ill-posedness and observation noise.

A.3 Predictive Checks with Bayesian p-Values

Using μ_{post} as boundary conditions in the finite element model allows us to compare the model predictions with observations. Figure A-1 provides a visual comparison of the modeled displacements (colors and light grey arrows) with the observed displacements for different time periods. Visually, there seems to be good agreement in both cases. However, the estimated boundary displacements are much larger over the 10 March – 12 March time period.

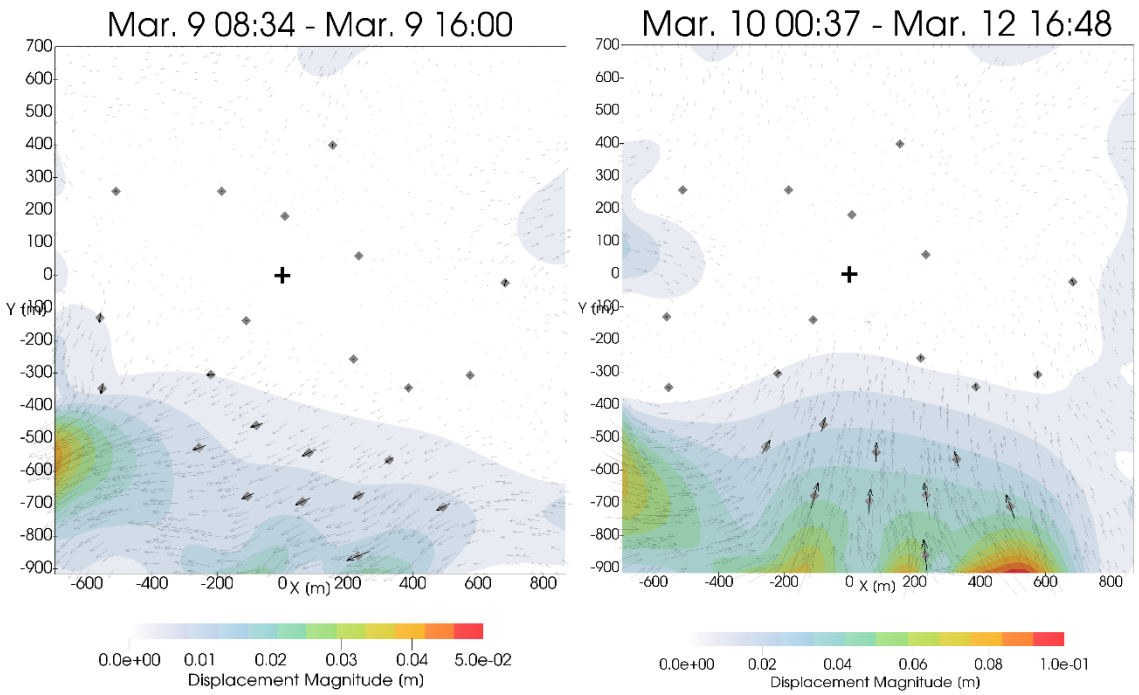

Figure A-1. Comparison of modeled and observed displacements. The black arrows correspond to observed displacements while the colors and light grey arrows are the mean model prediction. The black ``+" at (0,0) is the laser location. These correspond with Figures 6b and 9a in the main text, respectively.

To more quantitatively measure agreement of models and observations, we employ a quantitative posterior predictive check in the form of Bayesian p-values. See (Gelman & Shalizi, 2013) and (Kruschke, 2013) for a discussion on the Bayesian interpretation of p-values. The goal is to measure how "extreme" the observational data is under our modeling assumptions. Sufficient extremeness implies that our linear elastic model is a poor representation of reality and that non-elastic processes are likely at play. Propagating the posterior distribution on $\hat{u}_{bc}$ to the reflector displacements $\hat{u}_{ref}$ gives a Gaussian predictive distribution of

$$p(\hat{u}_{ref}|\hat{u}_{obs} = N(BK^{-1}\mu_{post}, BK^{-1}\Sigma_{post}K^{-T}B^T + \Sigma_\epsilon)$$

Let L be a Cholesky factor of this predictive covariance and consider summary statistic $\|L^{-1}\hat{u}_{obs}\|^2$. A Bayesian p-value is the the probability that a model prediction exceeds this quantity. If the p-value is small, it is unlikely for the model to predict more "extreme" values than the observations, thus indicating that the observations are in the tail of the predictive distribution and unlikely under the model assumptions. As reported in the main text, we obtained p-values of 0.3 for the 09 March time period and a much smaller p-value of 10^{-3} for the 10 March – 12 March time period. This indicates that our modeling assumptions (linear elasticity, Gaussian, etc.) are valid during the first time period, but not likely during the second despite the reasonable fit seen in Figure A-1.

References

Gelman, A., & Shalizi, C. R. (2013). Philosophy and the practice of Bayesian statistics. *British Journal of Mathematical and Statistical Psychology*, *66*(1), 8–38.

Kruschke, J. K. (2013). Posterior predictive checks can and should be Bayesian: Comment on Gelman and Shalizi,'Philosophy and the practice of Bayesian statistics.' *British Journal of Mathematical and Statistical Psychology*, *66*(1), 45–56.

Logg, A., Mardal, K.-A., & Wells, G. (2012). *Automated solution of differential equations by the finite element method: The FEniCS book* (Vol. 84). Springer Science & Business Media.

Rasmussen, C. E. (2003). Gaussian processes in machine learning. *Summer School on Machine Learning*, 63–71.